The Aeolian Environment of the Landing Site for the ExoMars Rosalind Franklin Rover in Oxia Planum, Mars

Journal Item

JGR Planets

RESEARCH ARTICLE

10.1029/2020JE006723

The Aeolian Environment of the Landing Site for the ExoMars Rosalind Franklin Rover in Oxia Planum, Mars

E. A. Favaro[1], M. R. Balme[1], J. M. Davis[2], P. M. Grindrod[2], P. Fawdon[1], A. M. Barrett[1], and S. R. Lewis[1]

[1]School of Physical Sciences, Open University, Milton Keynes, UK, [2]Department of Earth Sciences, Natural History Museum, London, UK

Key Points:

- Multiple wind regimes have influenced the surficial expression of Oxia Planum
- Transverse aeolian ridges (TARs), periodic bedrock ridges, dust devils, and windstreaks were used to determine formative wind directions
- Landscape evidence and climate modeling suggest contemporary winds lack the necessary strength to mobilize TAR-forming materials

Correspondence to:

E. Favaro,
elena.favaro@open.ac.uk

Citation:

Favaro, E. A., Balme, M. R., Davis, J. M., Grindrod, P. M., Fawdon, P., Barrett, A. M., & Lewis, S. R. (2021). The aeolian environment of the landing site for the ExoMars Rosalind Franklin Rover in Oxia Planum, Mars. *Journal of Geophysical Research: Planets*, *126*, e2020JE006723. https://doi.org/10.1029/2020JE006723

Received 4 OCT 2020
Accepted 22 JAN 2021

Abstract Aeolian features at Oxia Planum—the 2023 landing site for the ExoMars *Rosalind Franklin* Rover (ERFR)—are important for Mars exploration because they record information about past and current wind regimes, sand transport vectors, and lend insight to the abrasion, deposition, and transport of granular material. To characterize the wind regime and erosional history of Oxia Planum we used a combination of manual observational and machine-learning techniques to analyze the morphometrics, distribution, and orientation of 10,753 aeolian bedforms (Transverse Aeolian Ridges[TARs]) and landforms (Periodic Bedrock Ridges [PBRs]) around the ERFR landing ellipses. We found that, irrespective of the scale of the TARs, crestline azimuths are consistent across the study area and we infer that the bedform forming winds blew from NW-NNW toward SE-SSE. PBR azimuths show a substantively different orientation to the aeolian bedforms, and we infer that the winds necessary to abrade PBRs had a N-NNE or S-SSE orientation (180° ambiguity). From observations of active dust devils and windstreaks from repeat imagery, we infer a W-WNW or E-ESE (180° ambiguity) wind dominates today. Finally, we compare the inferred wind direction results from the aeolian landscape to modeled wind data from Mars Global Circulation Models. We note that, despite landscape evidence to the contrary, modeled contemporary wind direction lacks the consistent directionality to be responsible for the orientation of aeolian features in Oxia Planum. These results characterize aeolian features ERFR will encounter and suggests multiple wind regimes have influenced the surficial expression of the landing site.

Plain Language Summary Aeolian features like granular ripples and bedrock ridges provide important information about the wind regime in areas that lack long-term monitoring. Such is the case for Mars, and especially for Oxia Planum—the 2023 landing site for the ExoMars *Rosalind Franklin* Rover. This study examined the morphologies, distributions, and orientations of 10,753 ripples and ridges to understand the wind history at the landing site. We found that winds would have had to originate from substantively different directions to form the bedrock ridges than would be necessary to form the granular ripples. We also investigated contemporary wind signals with dust devils, dust devil tracks, and windstreaks, and found they too have a substantively different formative wind direction than the ripples and ridges. Modeled winds for the study area suggest contemporary winds lack the strength and directionally to be responsible for dust devils and windstreaks, suggesting at least two different wind epochs affected the region, and that current winds are not responsible for the expression of granular ripples or bedrock ridges. Our results help constrain the wind climate at the Oxia Planum landing site and suggest multiple wind regimes have affected the landing site.

1. Introduction

The surface of Mars is replete with evidence of extensive geomorphic modification by wind: dust devils (M. Balme & Greeley, 2006), centimeter-scale ripples (e.g., Lapotre et al., 2016, 2018), meter to decimeter-scale Transverse Aeolian Ridges (TARs; Bourke et al., 2006; M. Balme et al., 2008), periodic bedrock ridges (PBRs; Montgomery et al., 2012), wind streaks (e.g., P. Thomas et al., 1981), meter to kilometer-scale ventifacts and yardangs (e.g., Day et al., 2016; Kerber & Head, 2010; Mandt et al., 2008; Zimbleman et al., 2010), kilometer-scale dunes (e.g., Chojnacki et al., 2019; Hayward et al., 2014), and sand sheets (e.g., Runyon et al., 2017). Repeat, high-resolution orbital images and data from landers and rovers on the surface show that the sediment transport processes responsible for these aeolian features are currently active across much of the surface of Mars—a result of the interaction between surficial granular material and the thin Martian

atmosphere. Encoded in these aeolian features is information about paleo and contemporary wind regimes, erosion rates, and sediment production, availability, transport, and flux (J. M. Davis et al., 2020). Quantifying and qualifying aeolian signals is therefore important for understanding the martian environment across a continuum of spatial and temporal scales and is also vital for operating a surface mission efficiently and safely.

The European Space Agency's ExoMars *Rosalind Franklin* Rover (ERFR) and the surface platform element *Kazachok* are due to land at Oxia Planum (Vago et al., 2018) in 2023. The goal of ERFR is to search for signs of life on Mars and investigate the surface and subsurface geochemical environment (J. L. Vago et al., 2017). Over a nominal mission of ~218 Martian days, ERFR will explore Oxia Planum in search of biomarkers; the complex organic molecules uniquely formed by biological processes. Using the Panoramic Camera (PanCam; Coates et al., 2017) and other remote sensing instruments, ERFR will identify suitable targets for drilling. If rocks are exposed to the surface, they experience a high dose of cosmic radiation (Pavlov et al., 2002), damaging the structure of the organic compounds. To avoid this radiation damage, ERFR will drill to 2 m depth into the shallow subsurface to collect samples to be analyzed for organic compounds in the Pasteur instrument suite.

The identification of target rocks and subsequent analyses will only be possible if ERFR can sample rocks with the highest biomarker preservation potential. To do this, ERFR must be able to identify the correct targets and successfully traverse to those potential sample sites. For the analysis of these samples to be meaningful, we must understand the processes that might have affected the potential formation, concentration, and preservation of biomarkers. Understanding the paleo-environmental history recorded in the aeolian landforms in Oxia Planum, which may have influenced the formation of the rocks, as well as their possible erosion and exposure to the irradiating surface environment is therefore vital. Also, during previous rover missions, aeolian deposits have been a significant risk and limit on rover traversability (e.g., Arvidson et al., 2011, 2017). Consequently, the contemporary aeolian environment and deposits should be comprehensively characterized before rover operations.

Oxia Planum is located on the margin of Chryse Planitia and Arabia Terra (Figure 1a), and dates from the Noachian (Quantin-Nataf et al., 2020; Tanaka et al., 2014), potentially the most habitable period in martian history (Bibring et al., 2006; Carr et al., 2010). The landing ellipse lies on the edge of the regional north-trending slope of the Chryse-Arabia Margin (Figure 1). The basin floor is dominated by a phyllosilicate-bearing unit, with abundant spectral signature detections of Mg/Fe smectites (Figure 1c) throughout the landing ellipse, as well as local detections of Al-rich clays (Mandon et al., 2020). This material, which is identifiable throughout the circum-Chryse region (Carter et al., 2015) may represent the progressive chemical weathering of a layered basaltic parent rock. While these minerals indicate aqueous processes, the timing of the aqueous alteration and the origin of the host material exhibiting clay signatures in the landing ellipse is not yet known (Mandon et al., 2020; Quantin-Nataf et al., 2020). In the east of Oxia Planum are several sediment fans, situated at the end of Coogoon Valles (Figure 1). The Coogoon Valles fluvial system, which supplies sediment from an extensive catchment (Fawdon et al., 2019; Molina et al., 2017) has been active several times. The most recent sediment fans clearly postdating the phyllosilicate-bearing unit, implying that a period of subaerial erosion occurred between the two events (Quantin-Nataf et al., 2020).

Here, we describe the aeolian environment of the Oxia Planum landing site, as determined using orbital remote sensing data. Images from multiple orbital datasets reveal many examples of simple ripple-like bedforms (TARs) and linear PBRs at the landing site. The ubiquity of TARs across many regions of Mars make them ideal targets to study the coupling between the surface and atmosphere across the Martian surface (M. Balme et al., 2008; Berman et al., 2018). Additionally, their spatial distribution provides important information about sediment source availability, and transport. Note that we use the term Transverse Aeolian Ridge generically to describe morphologically simple, meter-scale or larger, wind-transverse granular ripple-like bedforms on Mars that are not superposed on dune forms, and which in almost all cases have not been observed to be actively migrating (although see Silvestro et al., 2020). TARs are commonly interpreted to form in a similar manner to terrestrial megaripples, as previous surface missions (i.e., Mars Exploration Rovers [MER] Spririt and Opportunity and Mas Science Laboratory [MSL] Curisoity; Achilles et al., 2017; Banham et al., 2018; N. Bridges et al., 2013; Ehlmann et al., 2017; Fenton et al., 2015; Goetz et al., 2010; Sullivan et al., 2005, 2008; Weitz et al., 2018) have shown that smaller TARs are typified by the accumulation

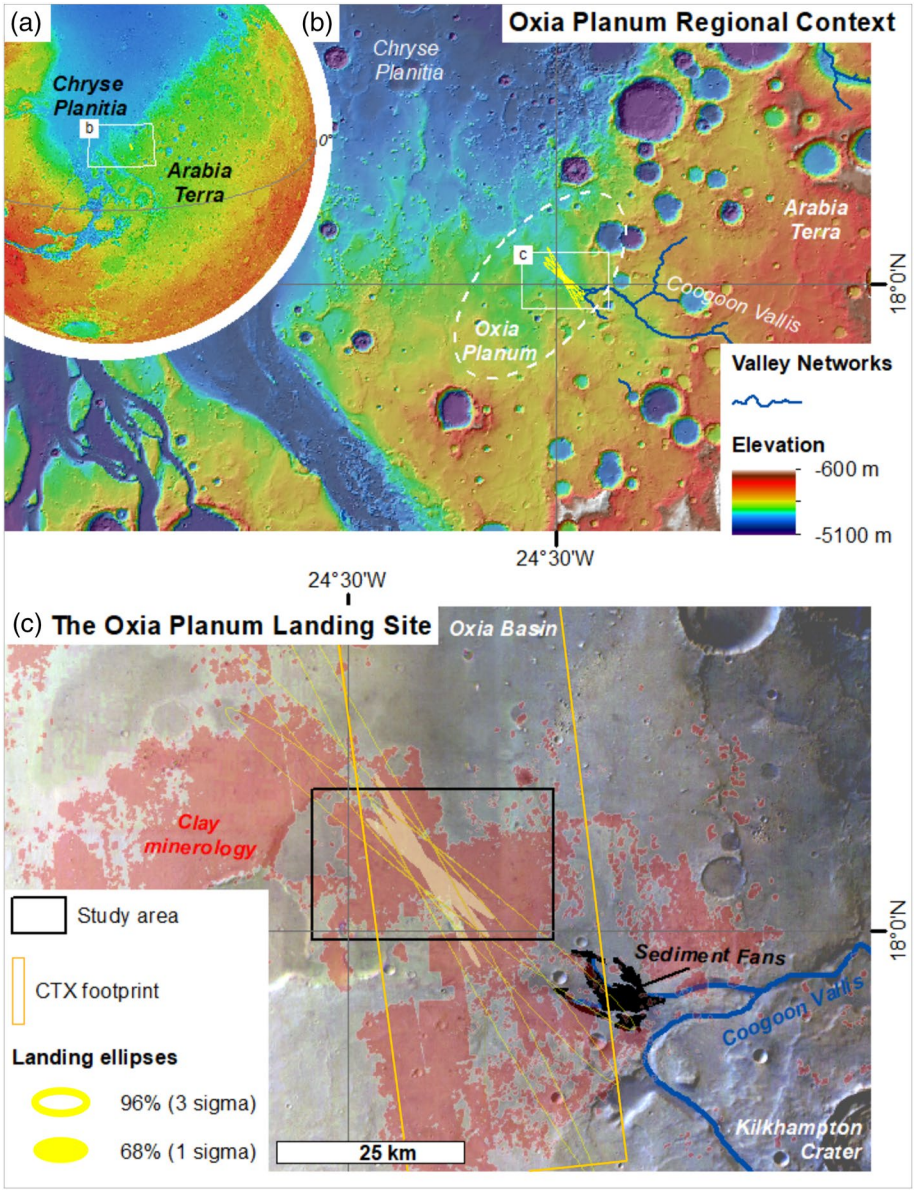

Figure 1. (a) Global and (b) regional context for Oxia Planum on the margin of Chryse Planitia and Arabia Terra. (c) The locations of the clay minerology detections (red shade in [c]), ERFR 2020 landing ellipses, CTX dust devil study footprint as shown in Figure 2, and 640 km^2 study area where data for this work was collected (black rectangle). ERFR, ExoMars *Rosalind Franklin* Rover; CTX, Context Camera.

of coarse grain material atop finer-grained material, which acts to armour the ripple. Some authors suggest dust accumulation atop TARs result in higher albedos relative to surrounding terrain, and may also denote inactivity (e.g., M. Balme et al., 2008; Berman et al., 2018). Also, analog studies on Earth show that megaripples can appear identical in form to Martian TARs (N. T. Bridges et al., 2015; de Silva et al., 2013; Hugenholtz & Barchyn, 2017; Hugenholtz et al., 2015; Milana, 2009; Zimbleman, 2010).

PBRs are meter- to decimeter-scale ridges eroded directly from bedrock substrate (Hugenholtz et al., 2015; Montgomery et al., 2012). Like TARs, PBRs are wind-transverse landforms (Montgomery et al., 2012) and therefore retain an important climatic signal. PBRs also lend insight to the depositional environment in which they, as layers of surface bedrock are abraded into the ripple-like forms seen in orbital images. Although both TARs and PBRs constitute potential rover traversability hazards during the mission phase of

the program (M. Balme et al., 2018), their morphology and spatial distribution nevertheless provide key climatological indicators which aid in characterizing the region.

In this study, we present new observations and measurements of aeolian surface features in a 640 km^2 study area in Oxia Planum (Figure 1c). We also present previously unpublished data describing the distribution of TARs in this area from the ERFR landing site selection and characterization process. This includes both measurements made using the NOvelty and Anomaly Hunter-HiRISE tool (NOAH-H; Balme et al., 2019) machine learning system, and results of a manual mapping exercise aimed at measuring TAR surface cover to determine the rover traversability of the site. We used further manual mapping to measure aeolian feature orientation and ridge lengths, combining the data to elucidate regional paleo and contemporary wind patterns in the study area. We used orthorectified and coregistered repeat High Resolution Imaging Stereo Experiment (HiRISE; Malin et al., 2007) imaging of a TAR field close to the study area to search for ongoing movement over 5 Martian years. Active dust devils were identified within the study area, and their speed and directionality mapped using High Resolution Stereo Camera (HRSC; Jaumann et al., 2007) and Color and Stereo Surface Imaging System (CaSSIS; J. Vago et al., 2015) images. Additionally, change detection between consecutive Context Camera (CTX; Malin et al., 2007) images was used to analyze any alteration in dust devil tracks and/or windstreaks on the surface to gain a better understanding of present-day wind conditions. In the absence of in situ near surface wind speed and direction data, we used Global Circulation Model (GCM) near surface winds derived from several contemporary re-analyses of spacecraft thermal and dust opacity data (Holmes et al., 2020) to obtain the best possible understanding of the current wind regime at Oxia Planum.

2. Methods

2.1. Manual Mapping of Aeolian Bedform Spatial Distribution

As part of the ERFR landing site characterization and selection process, we measured the distribution of aeolian bedforms for parts of each of the "final three" landing sites (Aram Dorsum, Mawrth Vallis and Oxia Planum; M. R. Balme et al., 2020; Poulet et al., 2020; Quantin-Nataf et al., 2020). Note that we only describe the results of the Oxia Planum study here. TARs and lower albedo, dune-like bedforms ("Low-albedo Dunes" [LDs]) were investigated, although no identification of LDs was made for Oxia Planum. Furthermore, because the study was intended to inform site traversability by the ERFR, only TARs with across-bedform lengths of more than ~2 m were considered: smaller bedforms were assumed to have ridge heights less than ~20–30 cm (M. Balme et al., 2018) and hence to provide a low traversability hazard. For this reason, the studies were limited to analyzing the distribution of moderate to large TARs, with the specific aim of providing an estimate of their fractional areal coverage over as large a part of each landing site as possible.

To measure TAR distribution, HiRISE images covering the site were imported into a Geographical Information Systems (GIS) and the study area split into a grid system of 2.5 × 2.5 km areas. Within each grid, the HiRISE data were examined at a scale of 1:2000 (less than half the native resolution, meaning that TARs smaller than 2 m across could generally not be seen), and patches of TARs with similar spatial coverage identified. We followed the definitions of M. Balme et al. (2008) who describe TAR spatial coverage as being "saturated"; "closely spaced" or "widely spaced", and used these guidelines to digitize around areas of TARs with approximately 100% (saturated), 50% (closely spaced), or 20% (widely spaced) spatial coverage. By mapping TAR patches in this way, large areas could be mapped many times more quickly than if digitizing bedforms individually. Digitizing was performed by a group of student volunteers and members of the research team, but as the whole team was trained to follow the same procedures and was collocated for most of the mapping exercise, the outputs were consistent across the different grids. When the TAR patches had been digitized, a simple GIS spatial calculation was used to display the geographical distribution of TAR spatial coverage as a 1 km square gridded summary product.

2.2. NOAH-H Characterization of Aeolian Ripples and Bedrock Classes

The NOAH-H system (Balme et al., 2019) was developed to characterize terrain types at the ExoMars candidate landing sites, using a machine learning approach. It is intended to form a key component of traversability analysis, when combined with topographic data and the engineering specifications of the rover. The

NOAH-H model is a deep learning neural network (DNN; He et al., 2016; LeCun et al., 2015; Simonyan & Zisserman, 2014). It classifies the terrain types within a HiRISE image into one of 14 ontological classes of which six cover different TAR-like bedform morphologies (referred to in the NOAH-H study simply as "ripples"). Note that the definitions and classifications used here are slightly different than the manual mapping, due to both the limitations of the methods and the goals of the different studies.

The NOAH-H bedform classes are divided into two broad categories: "discontinuous" and "continuous" TARs. Discontinuous TARs are features where the aeolian bedforms are separated from one another by areas of nonaeolian material. This includes bedforms which are isolated on the surface, and those which form part of a sparsely distributed patch, overlying nonaeolian material. The model was trained to identify three varieties of discontinuous TARs: large isolated bedforms (which can be identified discretely as zones of 100% coverage by aeolian material), and smaller fields of sparsely distributed TARs overlying bedrock and nonbedrock materials, respectively (similar to patches of "widely spaced" TARs in the manual mapping study). The continuous classes describe bedforms of various sizes and are defined as patches of TARs which merge downwind into one another, or which are separated only by areas of the same aeolian material which forms the bedforms. The model was trained to identify three forms of continuous TARs. Two of these consist of "large" and "small" bedforms with a simple sinuous morphology, the cut off between the two classes being a wavelength perpendicular to the ridge crest of ~5 m. The final class consisted of TARs with a "rectilinear morphology" where ridge-crests perpendicular to one another intersect to produce a grid-like form (cf. "networked" TAR description in M. Balme et al., 2008). This last class was only found in a very few isolated locations, and so is not relevant to the present study.

These classes, together with a variety of nonaeolian textures, were defined based on the prevalent surface textures found across Oxia Planum. Representative examples in ~1,500 image sections were then manually labeled and used to train the DNN. The output of the model consists of a classified raster image, with 2 m pixel cells, highlighting areas of each class. These data were used to generate summary areal coverage products in the same way as the manual mapping, although in the case of the NOAH-H method, both large and small bedforms were measured. Unlike for TARs, no single NOAH-H class was designed to detect PBRs, although their presence is often correlated with detections of the "rugged" and "fractured" NOAH-H bedrock classes (Balme et al., 2019).

2.3. Orientation and Bedform Crestline Measurement of TARs and PBRs

The manual and machine learning methods described above were designed to measure only the spatial distribution of the surface cover by aeolian bedforms at Oxia Planum. To extract directionality data, and to measure the distribution of PBRs, a different method was used, in which individual TARs and PBRs were digitized directly from HiRISE image data in a GIS. First, a 640 km^2 study area in Oxia Planum (Figure 1) was gridded into 2 × 2 km quadrants, with every second quadrant analyzed. HiRISE images cover 98% of the study area. Within each analyzed quadrant, 10 0.03 km^2 circular buffer regions were randomly constructed. Each buffer was created such that it lay wholly within the boundaries of each analyzed quadrant and did not overlap other buffers. Within buffered regions, TAR crestlines were manually digitized as continuous and discontinuous TARs, following the same descriptions as the NOAH-H study. Utilizing the rugged and fractured NOAH-H bedrock classes, morphological descriptions of martian (Montgomery et al., 2012) and terrestrial PBRs (in the Argentinian Puna region; Hugenholtz et al., 2015), and our own observations of bedrock crests in Oxia Planum, we identified and manually digitized PBRs within the buffered regions throughout the study area.

2.4. Analysis of Present-Day TAR Migration Rates

Multiple, repeat HiRISE imaging of the center part of the Oxia Planum landing site is lacking, so we searched for present day TARs in the two locations that offered the best temporal coverage (Figure 2). One location was near to the center of the landing ellipses, whereas the other location was close to, but outside of, the most southeasterly extent of the landing ellipses. We used well-validated methods to co-register and correlate images taken at different times (Table 1); this approach has previously been used to monitor many other active aeolian features on Mars and is well described by various authors (e.g., Ayoub et al., 2014; N. T.

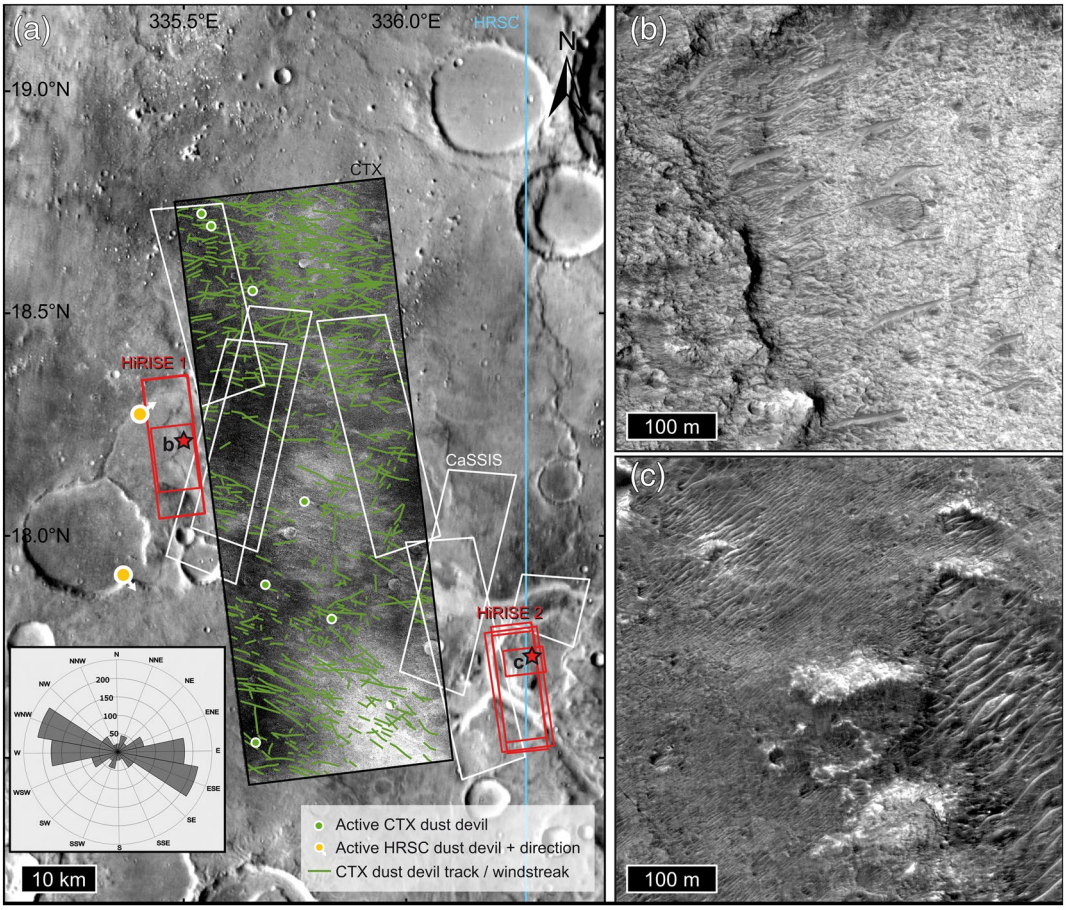

Figure 2. Analysis of present-day aeolian activity. (a) THEMIS daytime IR image mosaic with the location of study areas highlighted for HRSC (blue), CTX (black), CaSSIS (white), and HiRISE (red; PSP_009735_1985 and ESP_041211_1980, respectively). Also shown is the CTX subtraction image (J01_045167_1983—J03_045800_1983) used to identify dust devil tracks and/or windstreaks (green lines). Active dust devils identified in CTX (green circles) and HRSC (yellow circles with movement direction indicated by arrow) are also shown. Directional rose of dust devil/windstreak direction is noted in the inset image in (a). Values on the concentric circles denote frequency of occurrence. Orientation shows direction from which winds are inferred to blow. Red stars show the location of subsequent images. (b)–(c) Examples of area monitored for active aeolian transport using HiRISE data and COSI-Corr. CTX, Context Camera; HRSC, High Resolution Stereo Camera.

Table 1
HiRISE Images Used in the Analysis of Present-Day TAR Migration Rates

Location	Image	DTM?	Acquisition date	Relative time (Earth days)	Emission angle (°)
1	PSP_009735_1985	Y	August 24, 2008	0	8.4
	PSP_009880_1985	Y	September 4, 2008	11	7.8
	ESP_059303_1985		March 22, 2019	3,862	7.7
2	ESP_041211_1980	Y	May 12, 2015	0	10.9
	ESP_044890_1980		February 23, 2016	287	7.0
	ESP_049927_1980	Y	March 21, 2017	679	29.6
	ESP_050349_1980		April 23, 2017	712	0.2

Abbreviations: HiRISE,High Resolution Imaging Stereo Experiment; TAR,Transverse aeolian ridge

Bridges et al., 2012; Cardinale et al., 2016; Runyon et al., 2017; Silvestro et al., 2020, 2016). In summary, a stereo DTM was produced using the software packages ISIS and SocetSet, following standard procedures (J. M. Davis et al., 2020; Kirk, 2003; Kirk et al., 2008). This DTM was then used to co-register and orthorectify overlapping HiRISE images taken at different times. These orthoimages were imported into the software ENVI, where we carried out subpixel correlation with the plugin "Co-registration of Optically Sensed Images and Correlation" (COSI-Corr), which can detect surface displacements of between ~1/20 to 1/50 of a pixel (Leprince et al., 2007), and which has been used previously to predict minimum rates of movement through negative results (Grindrod et al., 2018). The correlation results for aeolian ripples were compared to bedrock regions, to determine whether any bedform movement was present above the inherent misregistration levels.

2.5. Analysis of Active Dust Devils

We used HRSC and CaSSIS images to determine the direction and velocity of any active dust devils in Oxia Planum. For HRSC, we used well-validated methods (e.g., Stanzel et al., 2006, 2008; Reiss, Raack, & Hiesinger, 2011; Reiss, Zanetti, & Neukum, 2011; Reiss et al., 2014) of tracking active dust devils through different images taken over the course of several minutes of the same observation. In this case, only a single HRSC observation (HF763_0000) was suitable and available but covered the majority of the landing ellipses. For CaSSIS, we checked stereo pairs taken about 1 min apart on the same orbit (N. Thomas et al., 2017). In this case, we used eight CaSSIS stereo image pairs taken between September 2018 and March 2019, which mostly covered the central to south-east regions of the ellipses (Figure 2). From these observations we were able to extract dust devil motion vectors, which are, at least on Earth (M. R. Balme et al., 2012), a reasonable proxy for the instantaneous wind field.

2.6. Analysis of Dust Devil Tracks and Windstreaks

We determined the direction of present-day winds by analyzing features on the surface that changed between consecutive CTX images; we infer these to be either dust devil tracks (e.g., Reiss et al., 2016) or windstreaks (e.g., P. Thomas et al., 1981, Figure 2; Table 2). We used a stereo CTX pair to produce a DTM using the same method as for the HiRISE DTMs, and then used this DTM to co-register and orthorectify images. Following previous techniques (e.g., Perrin et al., 2020; Reiss, Raack, & Hiesinger, 2011; Reiss, Zanetti, & Neukum, 2011), we used consecutive images to detect new features, or changes to features, that could be interpreted as the result of aeolian activity. To minimize possible false identifications due to differences in image brightness and contrast, we first balanced the images in the across-track direction. We then subtracted the later image from the earlier image, to emphasize any changes and any possible active dust devils. Although this method can be used to identify active dust devils, it does not yield a direction of movement. At CTX resolution, it is also possible that wind streak or dust devil track features that have not formed between images are instead just emphasized during this process, and this approach should be used only for wind direction, rather than formation time.

2.7. Mars Global Circulation Model Outputs

Wind conditions were extracted from the GCM at 1.5 m above the local surface of the study area and bilinearly interpolated in the horizontal from the regular model grid to a point at 18.2°N, −24.4°E. The GCM used for the experiments was that run by the Open University modeling group. This has a spectral dynamical core (Hoskins & Simmons, 1975) with an energy and angular momentum conserving vertical finite-difference scheme (Simmons & Burridge, 1981). Gas species and aerosols, such as water vapor and dust, are transported using a semi-Lagrangian advection scheme (Newman et al., 2002) with mass conservation (Priestley, 1993). The physical parameterizations used are those of the latest version of the Laboratoire de Météorologie Dynamique GCM (Forget et al., 1999) and have been developed in a long-standing collaboration with many groups. Data assimilation was conducted with an analysis correction scheme (Lorenc et al., 1991), developed for application to Mars as in Lewis et al. (2007). The GCM and assimilation procedure were the same as used to create the OpenMARS reanalysis database (Holmes et al., 2020), except that the GCM was run with increased vertical resolution (70 layers covering the altitude range 0–100 km) and data

Table 2
Images Used in the Analysis of Active Dust Devils, Dust Devil Tracks, and Windstreaks

Instrument	Image	DTM?	Acquisition date	Relative time (Earth days)	Emission angle (°)
CTX	J01_045167_1983	Y	March 15, 2016	0	1.5
	J03_045800_1983	Y	April 05, 2016	50	14.1
HRSC	HF763_0000	Y	June 19, 2016	–	–
CaSSIS	MY34_003806_019_1		September 30, 2018	–	11.3
	MY34_003806_019_2		September 30, 2018	–	11.1
	MY34_003893_018_1		July 10, 2018	–	11.0
	MY34_003893_018_2		July 10, 2018	–	11.7
	MY34_004085_162_1		October 23, 2018	–	12.4
	MY34_004085_162_2		October 23, 2018	–	10.5
	MY34_004172_162_1		October 30, 2018	–	11.1
	MY34_004172_162_2		October 30, 2018	–	11.3
	MY34_004925_019_1		December 31, 2018	–	11.3
	MY34_004925_019_2		December 31, 2018	–	11.1
	MY34_005012_018_1		July 1, 2019	–	12.1
	MY34_005012_018_2		July 1, 2019	–	11.3
	MY34_005378_162_1		February 6, 2019	–	12.6
	MY34_005378_162_2		February 6, 2019	–	11.8
	MY34_005664_163_1		March 1, 2019	–	11.4
	MY34_005664_163_2		March 1, 2019	–	12.3

were stored at hourly intervals over 669 Mars days (sols) covering each full Mars year (668.6 sols). The GCM was run with a triangular horizontal truncation at a total wavenumber 32, with nonlinear products calculated on a 3.75° × 3.75° grid and the hourly records made on a 5° × 5° grid for later interpolation to the output site. Several Mars years were also run at a truncation at wavenumber 42 (a 2.81° × 2.81° nonlinear products grid and a 3.75° × 3.75° record grid) to test the sensitivity of the results to the resolution of the topography, but this was not found to be significant at the location of the present study, where local slopes are relatively small.

Data shown from reanalyzes of 3 recent Mars Years (MY) and was derived from an assimilation of spacecraft data. The years are numbered according to the scheme of Clancy et al. (2000), which has become a de facto standard for spacecraft data intercomparisons. MY33 is a recent year, during which no global-scale dust storm occurred, but typical large storms occurred at high southern latitudes in northern hemisphere autumn and winter in a very similar pattern to previous years (Read et al., 2017). During MY33 the data assimilated into the GCM were thermal profiles and total column dust opacities as derived from retrievals (Kleinböhl et al., 2009) of limb soundings by the Mars Climate Sounder (MCS) instrument, aboard the Mars Reconnaissance Orbiter spacecraft (McCleese et al., 2007). To account for more extreme dust events we also selected MY 25, which includes a major global dust storm just after northern hemisphere autumn equinox, and MY26, which does not and is more similar to MY33 except for a smaller dust event in late northern winter, from the earlier part of the OpenMARS database period (Holmes et al., 2020). The data assimilated during MY25 and 26 were retrievals of nadir-sensed temperature profiles (Smith et al., 2000) and total column dust opacity (Smith, 2004) from the Thermal Emission Spectrometer instrument aboard the Mars Global Surveyor spacecraft.

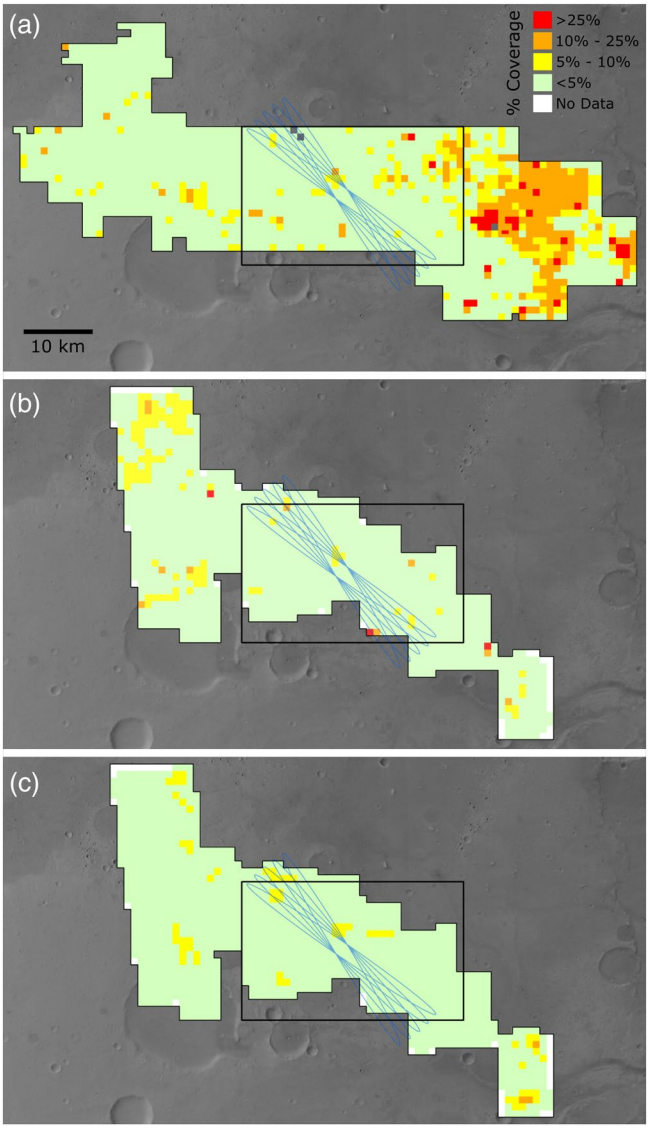

Figure 3. Examples of (a) a saturated TAR field in a 1830 m wide crater (ESP_042701_1985); (b) An 80 m wide crater with a dark, featureless floor, inferred to be sand filled (ESP_047501_1985); (c) Example of saturated small TARs (PSP_003195_1985); (d) Example of nonsaturated small TARs (ESP_041422_1985); (e) Example of PBRs (ESP_047501_1985). (f) Example of an upstanding mantled unit (a) atop bedrock (b) breaking down to form bedforms (c). There is a 2x vertical stretch applied to the DTM (HiRISE DTM made with ESP_037558_1985 and ESP_036925_1985). PBR, Periodic Bedrock Ridges; TAR, Transverse aeolian ridge.

3. Results

3.1. Observations and Distributions of Aeolian Features at the Oxia Planum Landing Site

Aeolian features present in the Oxia Planum landing site include TARs and PBRs (inferred to be of aeolian origin), but we have not observed any examples of duneforms. Neither have we observed any evidence of larger wind-parallel erosional features such as yardangs, although we acknowledge that ventifacts could be present but too small to see in remote sensing data. Possible local sandsheets (including morphologically featureless areas on plains and in craters) and apparently indurated surfaces that appear to be eroding to form aeolian bedforms are also common. Here we describe the key aspects of each type of aeolian feature.

3.1.1. Transverse Aeolian Ridges

TARs range in size from approximately a meter to a few tens of meters in across-bedform length, and occur in various settings. Larger (hundreds of meters in diameter) impact craters are commonly filled with saturated fields of larger TARs (e.g., Figure 3a). Smaller (tens to a few hundred meters diameter) craters can contain saturated TAR patches, or sometimes have a dark featureless floor, inferred to be windblown sand that has not formed bedforms (Figure 3b). Larger TARs (>5 m in across-bedform length) are found most commonly in local topographic lows and we have not seen any large fields of saturated decameter scale TARs outside of craters, although lone TARs or small patches of <10 bedforms of this size do occur. In contrast, extensive fields of smaller TARs (~5 m across or smaller, noting that image resolution makes it difficult to distinguish bedforms less than about 1 m across) form extensive fields covering the undulating plains of the landing site. These occur even outside of obvious topographic lows. These smaller TARs rarely form saturated fields of bedforms and there is nearly always bedrock or underlying regolith material visible between them (Figure 3c and 3d). Where TARs are large enough to distinguish tonal variations across them, we find that the flank northwest of the crest line is almost always lower albedo than the southeastern flank. The significance of this albedo difference is discussed in §4.1.

The distribution of percentage surface cover for TARs >2 m across, as measured by the manual digitization method, is shown in Figure 4a. The distribution of percentage surface cover for continuous TARs of all sizes, as measured by the NOAH-H system, is shown in Figure 4b. The distribution of percentage surface cover for noncontinuous TARs of all sizes, as measured by the NOAH-H system, is shown in Figure 4c, using the assumption that noncontinuous TARs have a 20% surface cover.

3.1.2. Periodic Bedrock Ridges

PBRs (Figure 3e) are characterized as fields of repeating, symmetrical bright linear ridges with an average length of ~67 m. They occur across the Oxia Planum, but most frequently in the south-central region of the study area in low relief areas. PBRs can be found in areas where granular material is not present, in areas where material has accumulated between ridges but does not coalesce into bedforms, or in areas where PBRs are partially covered by TARs. PBRs are also found on the floors of craters in the southern part of the study area and are overlain by intracrater granular material, often TARs. Craters, topographic lows, and fractures intersect PBR crestlines, exemplifying the cohesive nature of their substrate and differentiating them from the granular TARs.

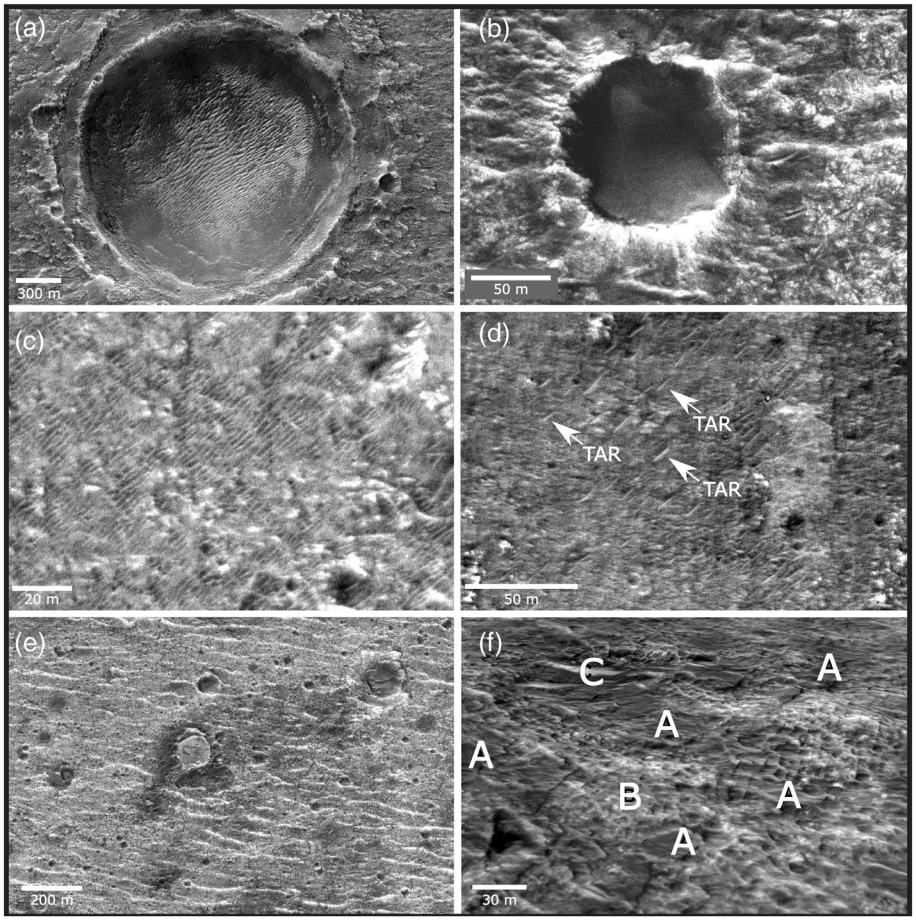

Figure 4. Results of TAR distribution measurements. (a) The distribution of TARs with across bedform length >2 m as measured using the manual mapping method. The data have been resampled to provide a 1 × 1 km grid in which the color-scale denotes the percent surface cover by TARs in that grid. Areas without data are shaded white, areas with no coloration were not sampled. The study area we used when measuring TAR and PBR ridge-crest directions (§2.3) is shown by the thin black box. (b) The distribution of continuous TARs in the study area as measured using the NOAH-H system. All other embellishments as per (a). (c) The distribution of noncontinuous TARs in the study area as measured using the NOAH-H system. 1-sigma probability uncertainty landing ellipses for the ERFR mission are marked by thin blue lines. Background is an HRSC nadir-pointing greyscale image mosaic. Image credits ESA/DLR/FUB. ERFR, ExoMars *Rosalind Franklin* Rover; HRSC, High Resolution Stereo Camera; NOAH-H, NOvelty and Anomaly Hunter-HiRISE tool; PBR, Periodic Bedrock Ridges; TAR, Transverse aeolian ridge.

3.1.3. Possible Sand Sheets and Indurated Low-Relief Surfaces

Patches of low albedo featureless terrain are commonly found within impact craters or other topographic lows. Where they have subtle "ripple-like" textures these are interpreted to be patches of wind deposited sand or, if instead piled against impact crater inner walls, as mass wasting deposits with grain size smaller than that of the resolution of the HiRISE images (~25 cm/pixel) (Figure 3b). However, in addition there are many moderate to low albedo patches with similar surface texture that appear to "drape" across bedrock surfaces (as shown by their higher albedo and crisp surface textures, including morphologies such as fracture patterns). These draping patches often have a distinct, well-defined scarp at their margins and show an abrupt contact with the material they superpose (e.g., Figure 3f). These mantling materials are probably less than ~1 m thick, as their relief cannot easily be seen in HiRISE DTMs. From these observations, we infer these materials to form indurated bodies, rather than loose sediment accumulations. Furthermore, many of these mid-albedo draping patches are associated with small TARs: many have small TARs on top of and around them.

Table 3
Summary Table Showing the Average Orientation and the Along-Crestline Length (L) Characteristics for Each Class of Aeolian Feature. n is the Number of Bedforms Measured

	n	Crestline length orientation[a]	L_{min} (m)	$L_{50\%}$ (m)	$L_{99\%}$ (m)	L_{max} (m)
Continuous TARs	7,989	60°/240°	1.1	7.0	11.4	57.9
Discontinuous TARs	2,764	61°/241°	1.1	12.2	108.0	556.0
Periodic Bedrock Ridges	457	98°/278°	4.1	67.4	371.1	601.5

[a]Accounting for 180° ambiguity.
Abbreviation: TAR, Transverse aeolian ridge.

3.2. Orientations of TARs and PBRs

We digitized and measured the along-crestline lengths and orientations of 7,989 continuous TARs, 2,764 discontinuous TARs, and 457 PBRs. TAR along-crestline lengths range from 1.1 to 556 m (Table 3). Meter-scale TARs are common across the study area, but decameter-scale TARs are uncommon. Irrespective of the scale of the bedform, we found crestline orientations for both continuous and discontinuous ripples to be consistent across the study area at 60°/240° and 61°/241° (accounting for 180° ambiguity), respectively (Figure 5). The 180° ambiguity is a result of the uncertainties in ascribing a bedform orientation without conclusive evidence of a formative wind direction. PBR along-crestline length ranged from 4.1 to 601.5 m (Table 3). They were found across the study area both on open plains and in craters. PBRs had a markedly different crestline orientation at 98°/188° (Figure 5), but again showed a very consistent trend across the study area.

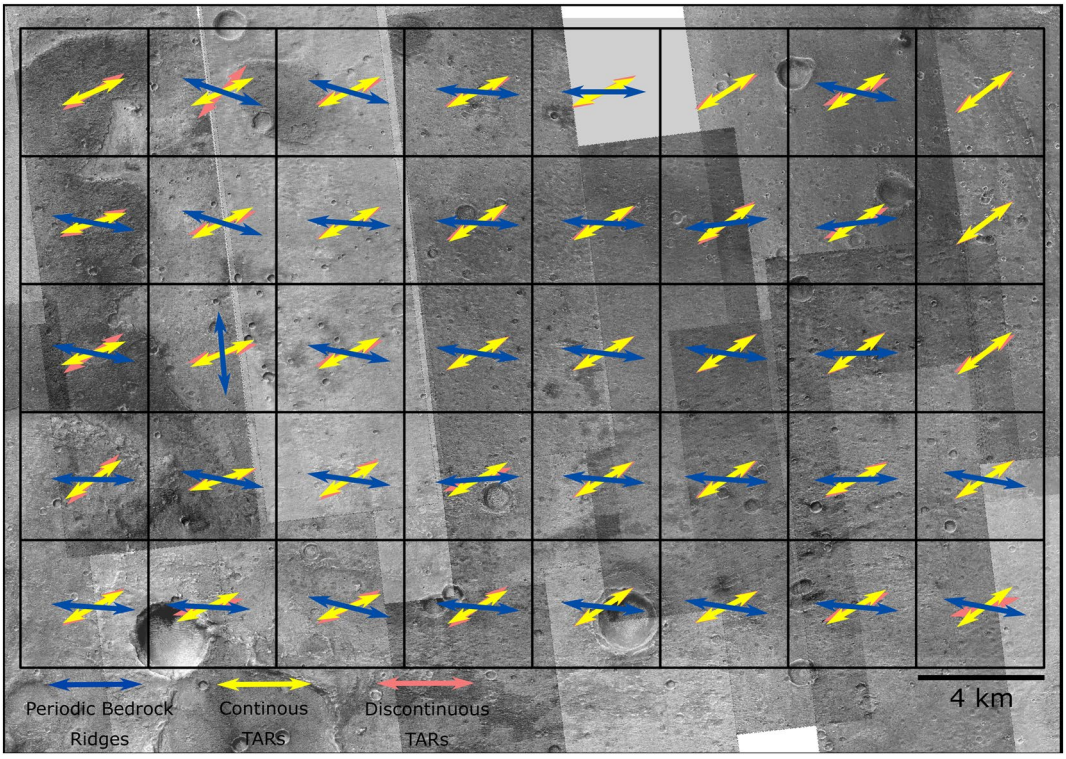

Figure 5. Map of average crestline orientation of PBRs and TARs within 4 × 4 km grids. PBR, Periodic Bedrock Ridges; TAR, Transverse aeolian ridge.

3.3. Present-Day Ripple Migration Rate

We did not identify any TAR or other aeolian feature in Oxia Planum that had definitively moved or changed between our HiRISE study images. The areas studied covered time periods of ∼2 and ∼11 Earth years (EY) for the south-east (SE) and central (C) areas respectively (Figure 2). Given the typical bedrock misregistration for both areas is ∼1 m, which is about twice that of normal aeolian studies using this technique (N. T. Bridges et al., 2012) the lack of movement observed allows us to place an upper bound to the maximum rate of TAR movement to ∼0.5 and ∼0.1 m/EY for the SE and C study areas. We conclude that if TARs are moving in this region, they are doing below our ability to detect their movement from orbit.

3.4. Multitemporal Observations of Active Dust Devils

We identified two active dust devils in multiple images taken during a single HRSC observation. These dust devils were ∼170 and ∼180 m in diameter, as measured in the nadir channel image (spatial resolution = 12.5 m/pixel). We observed these dust devils to have moved ∼1.5 and ∼1.4 km between the first and last images, resulting in respective velocities of ∼18 ms^{-1} for both features. The dust devils have moved generally toward the east, with the most clearly observed dust devil having moved in a NW-SE direction (∼141°), and the less obvious dust devil moving in a SW-NE direction (58°) (Figure 2). We conclude that the wind at this time was blowing toward the east. We identified no active dust devil movement between any of the CaSSIS stereo pairs that had been acquired at the time of writing.

3.5. Dust Devil Tracks and Windstreaks

We identified six further active dust devils that did not have multiple imaging and 649 dust devil tracks and/or windstreaks, that had appeared between the CTX image pair taken 50 Earth days apart, in an area covering 2,184 km^2 (Figure 2). These surface features had lengths ranging from 0.13 to 10.1 km, with a geometric mean of 1.83 km. The features are oriented predominantly in a WNW-ESE direction (with 180° ambiguity), with a geometric mean of 94°/274°, although there is a smaller secondary direction distribution of NNE-SSW (Figure 2). This direction is in agreement with the direction of the two active dust devils. The dust devils and dust devil tracks and/or windstreaks reached densities of up to 16 km^{-2} in some places to the north of the study area, with an overall mean density of ∼2.5 km^{-2} (Figure 6). Our observations are limited to a 50-day period, and therefore offer a snapshot of the contemporary wind regime. However, these features demonstrate the overall pattern of surface features that can be attributed to aeolian action. The center of this study region, which coincides roughly with the semi-major axes of the ellipses, showed the lowest densities of dust devil tracks and/or windstreaks.

3.6. Climate Model Output

We compared the GCM winds from the reanalysis at 1.5 m above the surface at Oxia Planum for MY 25, 26, and 33, and present their outputs in Figure 7. This permits comparison of 1 year with a global dust event (MY25) and two without, but which use assimilation of data from two different instruments and spacecraft (MY26 and MY33).

GCM predictions for all 3 years show variable directionality and the large-scale winds modeled explicitly in the GCM did not exceed 20 ms^{-1} (Figure 7). The strongest winds (up to 19 ms^{-1}) during each of the years originated from the north or south-east, except for a few strong winds over a range of angles centered on north-westerlies seen during MY25. The winds rotate through a range of angles on most days during each MY, with winds often less than 10 ms^{-1}. Simmilarly, an analysis of seasonality during these years (at Ls = 0/360, 90, 180, 270) reveal similar seasonal patterns typified by variable wind speed and direction that could not account for the orientation of aeolian features. There is a typically moderate wind speed and steady direction at night and peak winds in the early morning and late afternoon.

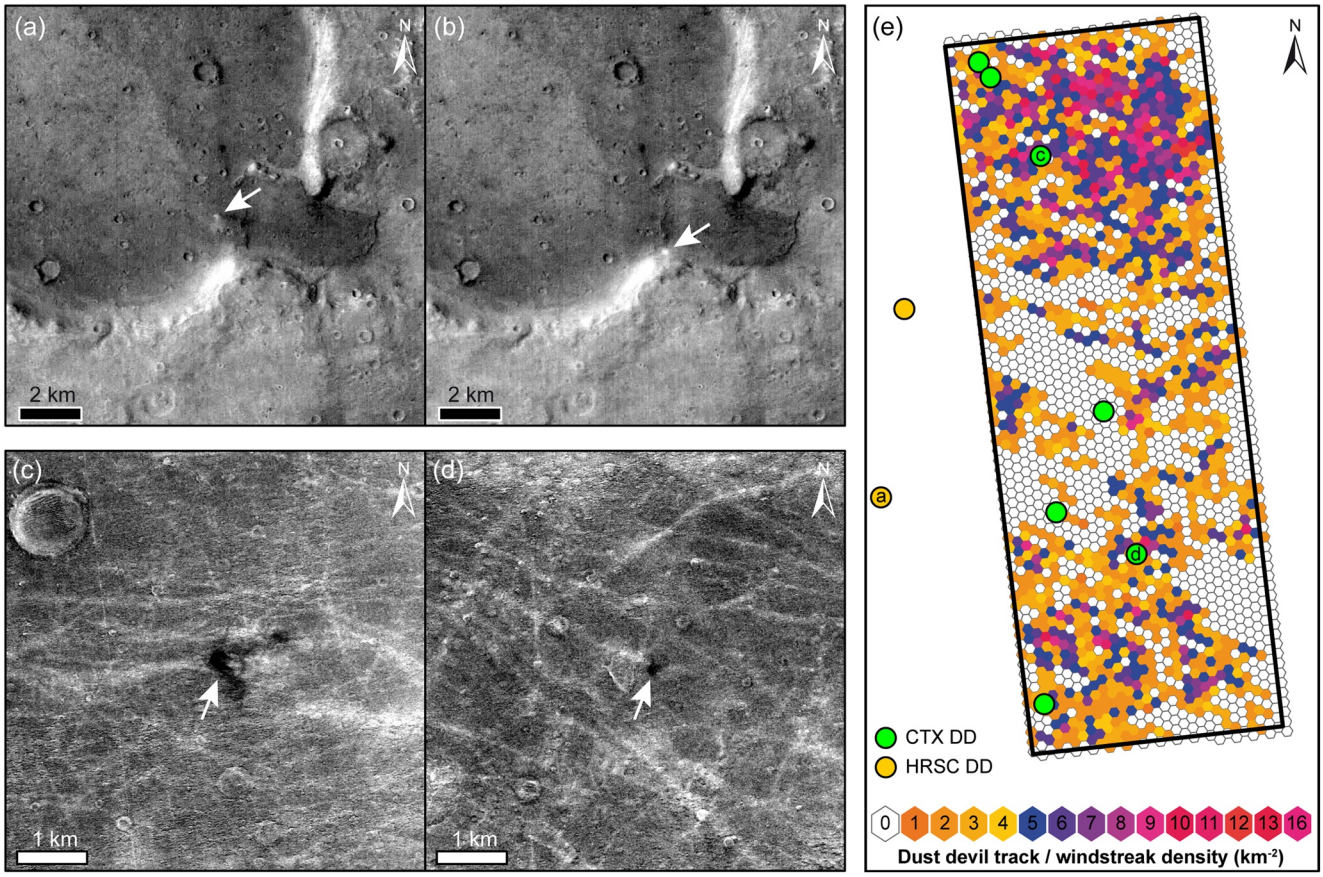

Figure 6. (a) Initial and (b) final location of an active dust devil observed in HRSC images (HF763_0000); (c) CTX image subtraction of J01_045167_1983 from (d) J03_045800_1983, noting the dust devil, with dust devil tracks/windsteaks also visible ([d] is original image); (e) Dust devil track/windstreak density map (km^{-2}) over the CTX image shown in Figure 1c (white outline) and Figure 2a. CTX, Context Camera; HRSC, High Resolution Stereo Camera.

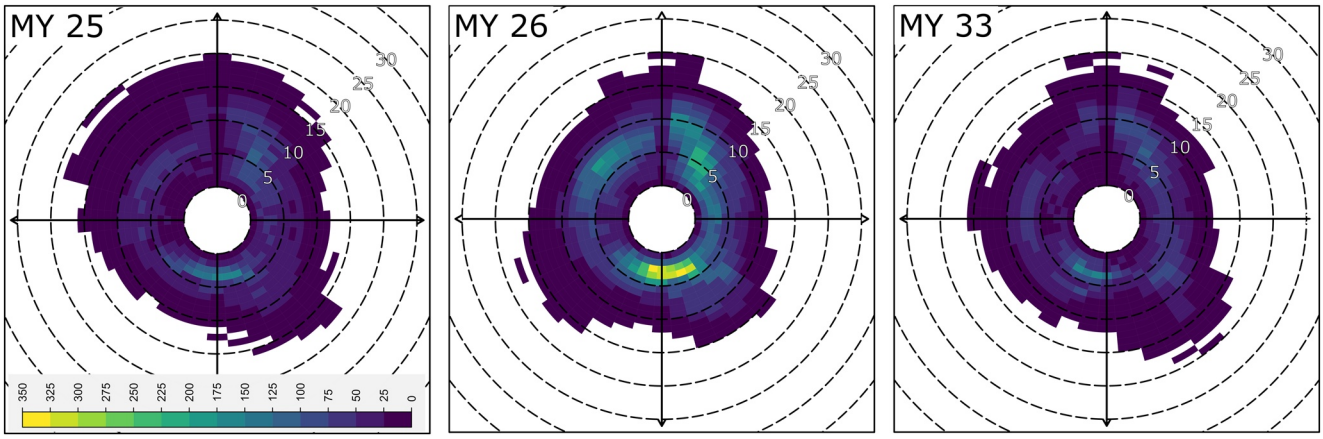

Figure 7. Modeled wind speed (ms^{-1}) and direction from GCM outputs for MY 25, 26, and 33. The color ramp denotes the frequency of an observation. The center ring of each plot represents a windspeed of 0 ms^{-1}. CTX, Context Camera; GCM, Global Circulation Model.

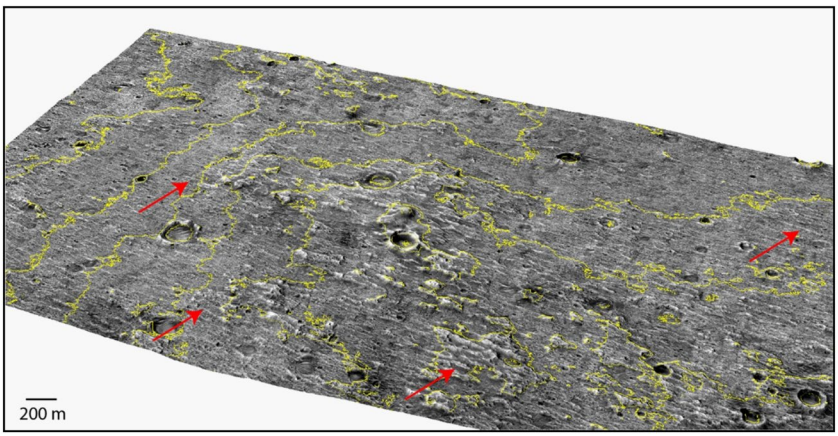

Figure 8. Perspective HiRISE image of PBRs in southern Oxia Planum. Note that the spacing of the ridges is consistent regardless of their topographic positioning (red arrows) and that they occur across multiple, distinct geologic units. These traits would not occur if the ridges were exhumed layered strata and are instead consistent with the interpretation that the ridges are PBRs formed into a palaeo-surface. Contours (yellow) are shown at 10 m intervals. HiRISE DTM made from stereo pair ESP_036925_1985 and ESP_037558_1985. HiRISE, High Resolution Imaging Stereo Experiment; PBR, Periodic Bedrock Ridge.

4. Discussion

4.1. Wind Regimes and Timescales of Aeolian Migration

4.1.1. Periodic Bedrock Ridges

Our analysis of PBRs across the study area highlights their approximately east-west (98°/278°) crestline orientation, and shows it is consistent across the study area (Figures 8 and 9). The observation that the PBRs host fractures shows that they are bedrock or lithified landforms, not granular bedforms. We offer three plausible formation hypotheses that could explain the origins of these features: (i) they are the surface expression of an extensive set of shallow-dipping bedrock layers, (ii) they are lithified TARs, formed perpendicular to the dominant winds, possibly buried, then re-exposed by regional-scale erosion, or (iii) they are erosional features, also formed perpendicular to the dominant wind, and again probably buried and re-exposed. Hypothesis (i) suggests the PBRs here were not formed by wind, but have been exposed by erosion (probably wind erosion), but in hypotheses (ii) and (iii) the PBRs would have formed transverse to the dominant winds, and also represent what must be a palaeosurface. We do not think the PBRs could be sets of lithified linear or transverse dunes, as their scale and morphology are dissimilar to linear dunes found on Earth and Mars (e.g., J. M. Davis et al. 2020; Tsoar, 1989)

We suggest that the PBR spacing and orientation, consistent across the study area irrespective of the aspect or slope of the undulating relief of the current surface, falsifies hypothesis (i). There is no subsurface configuration of layers that would be expressed at the surface in the observed pattern (Figure 8). We argue also that the consistent size, orientation, and spacing of the PBRs, and our observations of PBRs cutting across apparent changes in bedrock morphology, are inconsistent with a TAR interpretation. We would expect to see a wider variety of sizes and crest ridge patterns if these were indurated TARs. We cannot rule out this hypothesis, but feel that it is less likely to be true than the erosional PBR interpretation (hypothesis iii).

Erosional PBRs develop perpendicular to the dominant wind flow (Hugenholtz et al., 2015; Montgomery et al., 2012), signaling that the winds responsible for abrasion of PBRs at Oxia Planum would need to originate between N-NNE or S-SSW (Figure 9a). There is inherent ambiguity in our analysis of the formative wind direction necessary to abrade PBRs because HiRISE images of PBRs are not sufficient to resolve indicators of a stoss-lee pattern to the landforms (such as the difference in stoss-lee varnish seen on PBRs in Argentina [Hughenholtz et al., 2015]). Until in situ observations of PBRs can be made by ERFR, we are unable to definitively characterize the winds necessary for PBR development.

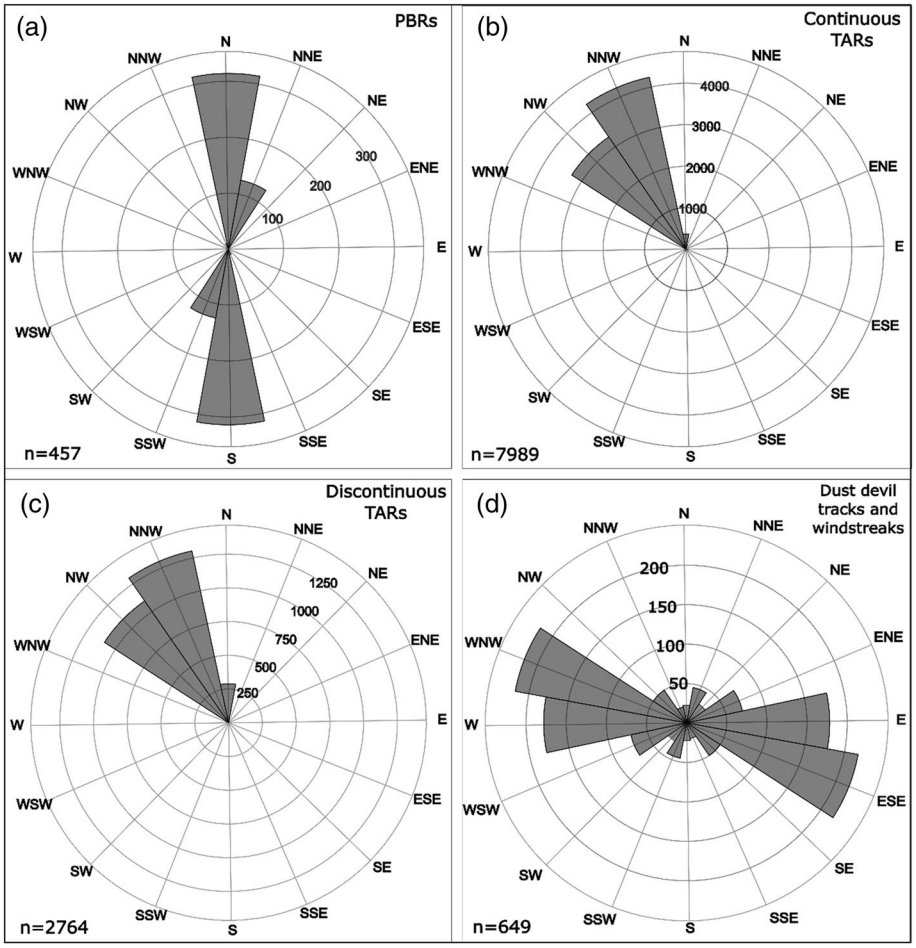

Figure 9. Directional roses for the formative winds responsible for (a) PBRs, (b) continuous and (c)discontinuous, and (d) dust devil tracks and/or wind streaks. Values on the concentric circles denote frequency of occurrence. Orientation shows direction from which winds are inferred to blow. PBR, Periodic Bedrock Ridges.

4.1.2. Transverse Aeolian Ridges

In our analysis of TARs across the study area, we found that the continuous and discontinuous TAR crestlines, irrespective of bedform size, were oriented roughly WSW to ENE (60°/240° and 61°/241°, respectively), denoting a formative wind from the NW-NNW or SE-SSE (Figures 7 and 9). To address the ambiguity in our azimuth calculations we used terrestrial analogs and remotely sensed albedo properties of TARs in Oxia Planum to determine the formative wind direction necessary for the observed TAR crestline orientation. In the Argentinian Puna, E. Favaro et al. (2020) confirmed that the color variation of megaripples seen in high resolution satellite images was due to the difference in grain accumulation across the bedform: the low-albedo megaripple stoss supported a sediment lag comprised of coarse (2–20 mm) particles (see also Milana, 2009) while the lee had a brighter albedo owning to the accumulation of smaller, saltation-amenable sand (0.063–2 mm) particles (Figure 10). TARs across Oxia Planum have a consistent albedo pattern that cannot be attributed to acquisition or sun angle. Therefore, based on the grainsize-albedo relationship of the Argentinian megaripples, and interpretations of TARs on Mars as having formed in the same way as megaripples on Earth, we posit that winds blowing from the NW-NNW to the SE-SSE were responsible for present-day TAR orientation (Figure 9)

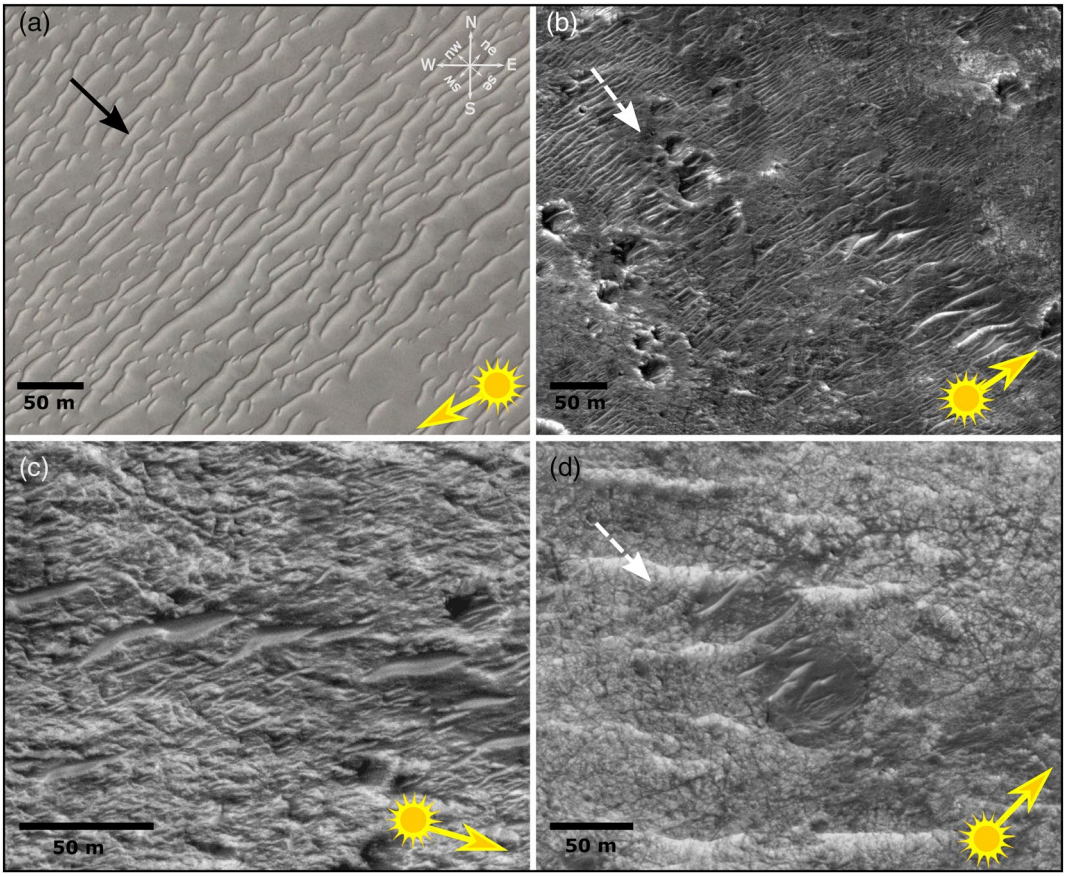

Figure 10. There are morphological and albedo similarities between (a) megaripples in the Argentinian Puna (26°36'35.51"S, 67°34'06.04") and (b)–(d) Oxia Planum (ESP_041422_1985, PSP_009735_1985, ESP_040433_1985, respectively). Using the grainsize-albedo relationship confirmed by E. Favaro et al. (2020) in Argentina, the stoss and lee slopes of TARs in Oxia Planum can be identified. This allows for characterization of the winds necessary to result in these orientations. The sun angle at time of image acquisition is also noted, demonstrating these albedo relationships are present in terrestrial and martian megaripples and TARs, respectively, irrespective of sun angle. TAR, Transverse Aeolian Ridges.

4.1.3. Comparison with Contemporary Winds and Climate Models

We found no evidence for movement of TARs under present day winds and estimate that TAR migration rates could not be more than 0.1–0.5 m/EY, in the unlikely event they are active. The modeled wind directions do not consistently agree with the geomorphic evidence of wind directionality from either the studied TARs or PBRs. Winds matching those with directionality responsible for PBR and TAR formation specifically, are not very strong nor sustained in the model output – which is necessary for the development of these features. The orientation of wind streaks and the migration paths of the observed dust devils sometimes align with the modeled winds, but they too lack consistency.

The aeolian landscape across Oxia Planum suggests the influence of multiple wind regimes over multiple timescales. The oldest wind is recorded in the N-S/S-N azimuthal orientation of PBRs. These erosional landforms coincide with the bedrock units identified by the NOAH-H system (Balme et al., 2019) and, in many cases, are overprinted with TARs and other granular deposits. If formed by wind, these PBRs formed on an ancient palaeosurface which, following the geological interpretation of the region (Quantin-Nataf et al., 2020), was likely Noachian or Hesperian in age.

The TARs, although unmoving over multiple Earth years, are indicative of a second, more recent wind regime which was dominated by northwesterly winds. Importantly, TARs of all scales and types show similar directionality. This suggests that the TARs here are not currently adjusting to a recently shifted wind

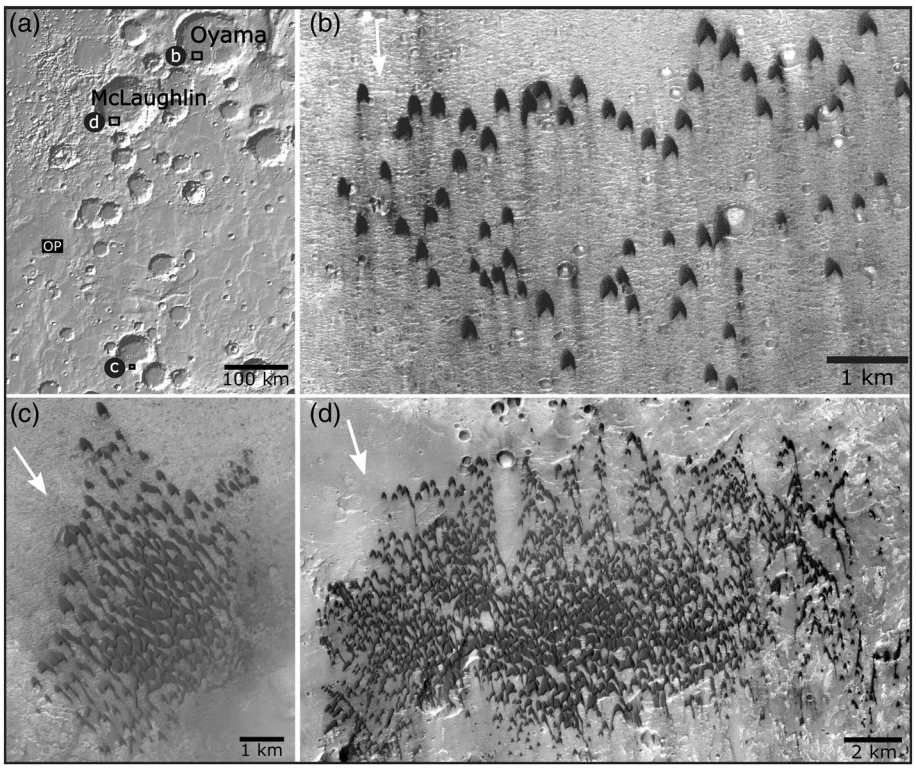

Figure 11. (a) Locations of the barchan dune fields in relation to the study area at Oxia Planum (OP), including (b) Oyama crater (CTX J18_051918_2034_XN_23N020W) where Chojnacki et al. (2019) identified barchan dunes migrating toward the southwest. (c) Barchan dunes in an unnamed crater southeast of the study area with their horns oriented toward the SE (CTX B19_016961_1970_XN_17N022W) and in (d) McLaughlin Crater with their horns oriented toward the SSE (CTX G22_026877_2017_XN_21N022W). White arrows denote formative wind directions necessary for dune morphology.

pattern, as in that case the smaller bedforms would adjust more quickly and show different orientations to the larger. This means that all the TARs in Oxia Planum are likely to be inactive, and that the current wind regime is not causing a readjustment of the bedforms here.

Morphological evidence from the migration and tracks associated with HRSC- and CTX-observed dust devils (e.g., Figure 6) suggest winds from the W-WNW and the E-ESE (180° ambiguity) currently blow through Oxia Planum.

Interpretation of GCM modeled outputs (Figure 7) for the study area are inconsistent with observations of wind directionality. Winds are realized from a multitude of directions, but their lack of consistency connotes natural variability and not necessarily an established pattern. It should also be noted that dust devil migration and their associated tracks and/or windstreaks may not be representative of the strongest contemporary winds in Oxia Planum as strong winds often preclude the ability of dust devils to form (e.g., Rafkin et al., 2016). If the strongest winds affect the region during Martian nights, we would be unable to track their directionality or speed as we do for those observed for this study (Figure 2). Overall, modeled outputs lack strong or consistent directionality or speed and are difficult to reconcile with observations of aeolian features found in the study area.

In the regions surrounding Oxia Planum, contemporary winds blowing from between NW and N are recorded in multiple dune fields (Figure 11). Chojnacki et al. (2019) note that barchan dunes ~415 km northeast of the study area in Oyama crater show migration toward the SE over four Martian years (Figure 11b); In McLaughlin crater (~225 km northeast; Figure 11c), and in an unnamed crater (~223 km southeast; Figure 11d) in Arabia Terra, the horns and slipfaces of the barchanoid dunes point toward the SSE-S and SE,

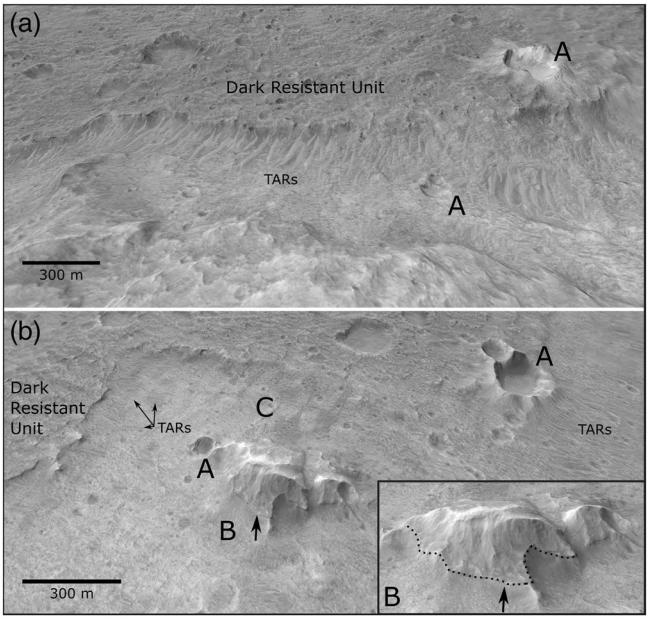

Figure 12. (a) The dark resistant material found in the western part of the study area (A) may be the source for the granular material which makes up the TARs and infills topographic lows.(b) Area surrounding an eroded mound where a clear boundary between two units is noted (dashed line in inset). In the inset image, the fractured clay unit (B) is exemplified. This mound is found adjacent to the same dark resistant unit as (a) and next to an example of eroding upstanding mantled units (C). There is a 5x vertical stretch applied to the DTM in (a) and a 2x vertical stretch applied to the DTM in (b) (both HiRISE DTMs made with PSP_009880_1985 and PSP_009735_1985). HiRISE, High Resolution Imaging Stereo Experiment; TAR, Transverse Aeolian Ridges.

respectively. The wind directions recorded by these barchans most closely align with the bedrock evidence at the landing site, but not the granular TAR and dust devil records.

4.2. Sediment Transport in Oxia Planum

Sediment transport is an important process to consider in terms of the greater ExoMars mission as well as deciphering the landscape evolution and climatic histories of Oxia Planum.

Erosion and deflation of granular material is important to the overall ExoMars mission as these processes are responsible for the exhumation of the clay-bearing units (Figure 1c). Extensive mapping of Oxia Planum using OMEGA (Visible and Infrared Mineralogical Mapping Spectrometer) and Compact Reconnaissance Imaging Spectrometer for Mars (Quantin-Nataf et al., 2020) show extensive mid-Noachian clay-bearing units (Quantin-Nataf et al., 2020; Tanaka et al., 2014). These clay-bearing units are critical regions for the EFER mission as they are the regions most likely to preserve biomarkers.

Across the study area, the lack of visible small TAR direction readjustment and lack of observed large TAR movement, coupled with low modeled wind speeds, suggest that the magnitude of contemporary winds is currently insufficient for TAR migration in Oxia Planum. However, we recognize dust devil activity in the study area which suggests that while winds are incapable of mobilizing TAR-forming material, dust can be transported regionally. We acknowledge that localized sand transport may occur locally (cf., Metzger et al., 2011; Raack et al., 2018) and be unresolvable from orbit.

Sediment transport is also evidenced by the erosion and deflation of thin, friable upstanding mantle units (Figures 3f and 12), found extensively in Oxia Planum, and a dark resistant unit in the northwestern part of the study region (Figure 12). Surrounding these units, extensive ripples and patches of sediment are found. It is unclear if the abrasion of these units is the provenance of the granular material, but their conjoined appearance suggests deflated materials from these units contribute to the sediment supply in Oxia Planum, which can then collect in topographic lows or coalesce into bedforms. Further evidence of erosion is evident in the morphology of buttes and mounds in the study region, which occur infrequently within the landing ellipses but extensively in the larger Chryse Planitia region (McNeil et al., 2020). Figure 12b is an example of a mound in the western part of the study area. The rounded morphology is indicative of erosion, and it displays a clear boundary between an upper unit, which resembles the dark resistant unit to its west, and the extensively exposed fractured clay material which lies below. Bedforms and granular deposits can be found proximal to this mound, and others in the study area, again suggesting that the erosion of these units could be a source of granular material. Additionally, if the upper portion of Figure 12b is the same material as the dark resistant unit to its west, the erosion of this mound, and others like it in Oxia Planum, could provide an estimate as to the volume of material eroded in the region, which have almost certainly been removed by aeolian processes.

Based on our TAR analysis and our hypothesis that the erosion of capping units sheds granular material that collects in topographic lows or coalesces into bedforms, we suggest erosion at Oxia Planum could be an intermittent process (e.g., high magnitude and low frequency events), or that erosion occurs as such a slow rate we are currently unable to accurately detect it.

4.3. Relevance to Rover Mission: Testable Hypotheses

While the overall goal of the ExoMars mission is to determine if life ever existed on Mars, the surface mission of the ERFR is well positioned to address aeolian questions that have vexed planetary geologists and geomorphologists for decades.

4.3.1. Sediment Transport and Grainsize Analysis

A qualitative and quantitative assessment of sediment transport across Mars is an open research question and one which still requires a great deal more data to constrain. The suite of high-resolution cameras onboard ERFR are well positioned, both physically onboard the rover and strategically in a larger mission context, to help address these questions.

The Close-Up Imager (CLUPI) camera is located on the underside of the ERFR main body, adjacent to the drill system. It is specifically designed to capture high-resolution (up to 7 μm/pixel) color images for close-up observations of regolith, rocks, and drill samples (Josset et al., 2017). CLUPI data can be used to conduct grainsize analyses of regolith both from the surface and brought up from the subsurface by the drill, and of ripples and sand deposits in the vicinity of the rover. Similar work of manually digitizing grains has been performed on images captured by the Mars Hand Lens Imager onboard Mars Science Laboratory *Curiosity* to determine the grain properties (size, shape, composition, etc.) of aeolian deposits, including dunes and ripples in Gale Crater (i.e., Achilles et al., 2017; Banham et al., 2018; Ehlmann et al., 2017; Weitz et al., 2018 among others). In addition to grainsize analysis, sediment transport studies can be undertaken by CLUPI. If the ERFR is stationary over several martian sols, repeat imagery of the surface should be used to determine if and where grains are moving, similar to how Mastcam images from *Curiosity* rover were analyzed by M. Balme et al. (2018).

The PanCam suite of cameras—including the high-resolution (HRC) and wide-angle cameras (WAC)—are situated on the camera bench atop a 1.4 m deployable mast and are well positioned to take geological context images of the areas surrounding the rover (Coates et al., 2017). From submillimeter resolution with HRC to meter resolution with WAC, images of TARs and PBRs can be acquired and studied on both a granular and bedrock scale, respectively, and at a wider landscape-context scale. WAC images, supported by lower-resolution images from the navigational cameras (NavCam) will be able to generate 3D digital terrain models of the landscape, which can then be analyzed for any number of scientific objectives, including rover traversability assessments, or simply to better understand crest heights and flank slopes (e.g., M. Balme et al., 2018). An objective of the PanCam team should be to build a database of aeolian features at multiple scales to reconcile remotely sensed data with in situ measurements. Specifically, repeat images of TARs can be used to identify particle movement along TAR crestlines to better understand if TARs are active and move below the current threshold for detection by satellite platforms, or if the winds in Oxia Planum are currently insufficient to mobilize the grains necessary for TAR migration. A TAR database can also be used to compare the TARs seen at Oxia Planum with those encountered along the *Curiosity* traverse, as well as the databases of aeolian bedforms collated by the Mars Exploration Rover missions (i.e., Achilles et al., 2017; Banham et al., 2018; N. Bridges et al., 2013; Ehlmann et al., 2017; Fenton et al., 2015; Goetz et al., 2010; Sullivan et al., 2005, 2008; Weitz et al., 2018) to compare their morphometrics, development, granulometry, and so on. This will help explain whether all simple ripple-like forms on Mars are formed by similar processes. Comparison of PBRs to those found elsewhere on Mars and Earth could help reconcile our observations of PBRs with theories of their development. Specifically, for PBRs at Oxia Planum, identification of stoss and lee slopes to the PBR through images of their crestlines would constrain the wind direction needed to form these landforms.

4.3.2. Mission Objectives While the Rover is Driving

With the widespread occurrence of TARs in Oxia Planum, it is likely that the ERFR will be required to traverse through smaller TARs as it makes its way to various targets. When the rover disrupts the TAR, CLUPI and HRC can photograph the wheel tracks and cross-sections of the disturbed ripple to ascertain granulometry of the bedform, similar to how images were acquired in 2005 during Opportunity's traverse

of Purgatory Ripple (i.e., Arvidson et al., 2011; Squyres et al., 2006). Determining granulometry will test the megaripple hypothesis of TARs, further characterizing these bedforms as either similar to terrestrial megaripples or a separate bedform class.

While the rover is on a traverse, the Water Ice and Subsurface Deposit Observation on Mars (WISDOM) ground-penetrating radar (GPR) (J. L. Vago et al., 2017) can conduct GPR surveys of the ripples to determine if wind reversals in Oxia Planum are recorded in the stratigraphy of the ripple itself or if there is evidence of other geomorphic factors (i.e., fluvial/alluvial) influencing the expression of the landscape. A similar methodology was used by Milana and Kröhling (2017) in the Argentinian Puna on gravel ripples, wherein they identified an epoch where alluvial processes influenced this now-aeolian dominated landscape.

5. Conclusions

We provide evidence for a dynamic wind regime, active on multiple timescales, at Oxia Planum. We do this by carefully examining and interpreting the action of the wind recorded on transverse aeolian ridges (TARs), PBRs, dust devils, and wind streaks. We compare the observational evidence with global circulation model (GCM)-derived wind patterns.

1. The oldest wind direction is recorded in the rock record through the orientation of PBRs. Based on their azimuths, they required either N-NNE or S-SSE blowing winds (accounting for 180° ambiguity) to develop. Clarification on formative winds may come if the ERFR lands close enough to PBRs to image their crestlines and determine stoss and lee slopes
2. Evidence of a second wind epoch is preserved in the TARs found throughout the study area. Irrespective of size, TARs have a consistent azimuth orientation, requiring winds blowing from the NW-NNW toward the SE-SSE
3. The contemporary wind regime, indicated by dust devils and windstreaks suggests winds blow from the WNW toward the ESE, and infrequently from the NNE toward the SSW
4. Additionally, through the coregistration of repeat HiRISE images, we have determined that TARs are immobile over ∼2 and 11∼ Earth years (EYs) (Figure 2), suggesting contemporary winds lack the necessary strength to mobilize TAR-forming materials. In addition, dust can be transported locally by dust devil action
5. In situ data from ERFR will further provide evidence for characterizing the aeolian environment and can be accomplished without negatively impacting the broader ExoMars mission objectives of locating traces of life at Oxia Planum

Data Availability Statement

GIS data products and data sets used to analyze TARs, PBRs, and dust devils/windstreaks are available for download online (Favaro and Grindrod, 2020). The standard data products used here are available from the NASA PDS (https://pds.jpl.nasa.gov/). The CTX DEMs and coregistered time series images are available for download online (J. Davis, 2019).

Acknowledgments
We thank Mariah Baker and Mark Bishop for their thorough and thoughtful review of this work, which improved the manuscript. EAF and MRB gratefully acknowledge UK Space Agency (UK SA) funding (ST/T002913/1, ST/V001965/1 and ST/R001413/1). JMD acknowledges UK SA funding (ST/R002355/1). PMG acknowledges UK SA funding (ST/R002355/1, ST/V002678/1, ST/L006456/1). PF acknowledges UK SA funding (ST/V001965/1 and ST/R001413/1). AMB and MRB acknowledge funding from the UK Science and Technology Facilities Council (STFC; grant ST/T000228/1), by a European Space Agency contract (4000118843/16/NL/LvH1145—Novelty or Anomaly Hunter (NOAH)), and by UK SA funding (ST/T000228/1). SRL acknowledges UK SA funding (ST/T002913/1, ST/R001405/1 and ST/S00145X/1). CaSSIS is a project of the University of Bern funded through the Swiss Space Office via ESA's PRODEX program. The instrument hardware development was also supported by the Italian Space Agency (ASI) (ASI-INAF agreement no. I/018/12/0), INAF/Astronomical Observatory of Padova, and the Space Research Center (CBK) in Warsaw.

References

Achilles, C. N., Downs, R. T., Ming, D. W., Rampe, E. B., Morris, R. V., Treiman, A. H., et al. (2017). Mineralogy of an active eolian sediment from the Namib dune, Gale crater, Mars. *Journal of Geophysical Research: Planets*, *122*(11), 2344–2361. https://doi.org/10.1002/2017JE005262

Arvidson, R. E., Ashley, J. W., Bell, J. F., Chojnacki, M., Cohen, J., Economou, T. E., et al. (2011). Opportunity Mars Rover mission: Overview and selected results from Purgatory ripple to traverses to Endeavor crater. *Journal of Geophysical Research*, *116*(E7). https://doi.org/10.1029/2010JE003746

Arvidson, R. E., Iagnemma, K. D., Maimone, M., Fraeman, A. A., Zhou, F., Heverly, M. C., et al. (2017). Mars science laboratory curiosity rover megaripple crossings up to sol 710 in gale crater. *Journal of Field Robotics*, *34*(3), 495–518.

Ayoub, F., Avouac, J. P., Newman, C. E., Richardson, M. I., Lucas, A., Leprince, S., & Bridges, N. T. (2014). Threshold for sand mobility on Mars calibrated from seasonal variations of sand flux. *Nature Communications*, *5*(1), 1–8. https://doi.org/10.1038/ncomms6096

Balme, M., Berman, D. C., Bourke, M. C., & Zimbelman, J. R. (2008). Transverse aeolian ridges (TARs) on Mars. *Geomorphology*, *101*(4), 703–720. https://doi.org/10.1029/2005RG000188

Balme, M., & Greeley, R. (2006). Dust devils on Earth and Mars. *Reviews of Geophysics*, *44*(3). https://doi.org/10.1029/2005RG000188

Balme, M. R., Barrett, A. M., Woods, M., Karachalios, S., Joudrier, L., & Sefton-Nash, E. (2019). NOAH-H, a deep-learning, terrain analysis system: Preliminary results for ExoMars Rover candidate landing sites. *In Lunar and Planetary Science Conference*, *2132*, 3011.

Balme, M. R., Gupta, S., Davis, J. M., Fawdon, P., Grindrod, P. M., Bridges, J. C., et al. (2020). Aram Dorsum: An extensive Mid-Noachian Age fluvial depositional system in Arabia Terra, Mars. *Journal of Geophysical Research: Planets*, *125*(5), e2019JE006244. https://doi.org/10.1029/2019JE006244

Balme, M. R., Pathare, A., Metzger, S. M., Towner, M. C., Lewis, S. R., Spiga, A., et al. (2012). Field measurements of horizontal forward motion velocities of terrestrial dust devils: towards a proxy for ambient winds on Mars and Earth. *Icarus*, *221*(2), 632–645. https://doi.org/10.1016/j.icarus.2012.08.021

Balme, M., Robson, E., Barnes, R., Butcher, F., Fawdon, P., Huber, B., et al. (2018). Surface-based 3D measurements of small aeolian bedforms on Mars and implications for estimating ExoMars rover traversability hazards. *Planetary and Space Science*, *153*, 39–53. https://doi.org/10.1016/j.pss.2017.12.008

Banham, S. G., Gupta, S., Rubin, D. M., Watkins, J. A., Sumner, D. Y., Edgett, K. S., et al. (2018). Ancient Martian aeolian processes and palaeomorphology reconstructed from the Stimson formation on the lower slope of Aeolis Mons, Gale crater, Mars. *Sedimentology*, *65*(4), 993–1042.

Berman, D. C., Balme, M. R., Michalski, J. R., Clark, S. C., & Joseph, E. C. (2018). High-resolution investigations of transverse aeolian ridges on Mars. *Icarus*, *312*, 247–266. https://doi.org/10.1016/j.icarus.2018.05.003

Bibring, J. P., Langevin, Y., Mustard, J. F., Poulet, F., Arvidson, R., Gendrin, A., et al. (2006). Global mineralogical and aqueous Mars history derived from OMEGA/Mars Express data. *Science*, *312*(5772), 400–404. https://doi.org/10.2307/3845879

Bourke, M. C., Balme, M., Beyer, R. A., Williams, K. K., & Zimbelman, J. (2006). A comparison of methods used to estimate the height of sand dunes on Mars. *Geomorphology*, *81*(3–4), 440–452. https://doi.org/10.1016/j.geomorph.2006.04.023

Bridges, N. T., Ayoub, F., Avouac, J. P., Leprince, S., Lucas, A., & Mattson, S. (2012). Earth-like sand fluxes on Mars. *Nature*, *485*(7398), 339–342. https://doi.org/10.1038/nature11022

Bridges, N., Geissler, P., Silvestro, S., & Banks, M. (2013). Bedform migration on Mars: Current results and future plans. *Aeolian Research*, *9*, 133–151.

Bridges, N. T., Spagnuolo, M. G., de Silva, S. L., Zimbelman, J. R., & Neely, E. M. (2015). Formation of gravel-mantled megaripples on Earth and Mars: Insights from the Argentinean Puna and wind tunnel experiments. *Aeolian Research*, *17*, 49–60.

Cardinale, M., Silvestro, S., Vaz, D. A., Michaels, T., Bourke, M. C., Komatsu, G., & Marinangeli, L. (2016). Present-day aeolian activity in Herschel Crater, Mars. *Icarus*, *265*, 139–148. http://dx.doi.org/10.1016/j.icarus.2015.10.022

Carr, M. H., & Head, J. W., III (2010). Geologic history of Mars. *Earth and Planetary Science Letters*, *294*(3–4), 185–203.

Carter, J., Loizeau, D., Mangold, N., Poulet, F., & Bibring, J. P. (2015). Widespread surface weathering on early Mars: A case for a warmer and wetter climate. *Icarus*, *248*, 373–382.

Chojnacki, M., Banks, M. E., Fenton, L. K., & Urso, A. C. (2019). Boundary condition controls on the high-sand-flux regions of Mars. *Geology*, *47*(5), 427–430. https://doi.org/10.1130/G45793.1

Clancy, R. T., Sandor, B. J., Wolff, M. J., Christensen, P. R., Smith, M. D., Pearl, J. C., et al. (2000). An intercomparison of ground-based millimeter, MGS TES, and Viking atmospheric temperature measurements: Seasonal and interannual variability of temperatures and dust loading in the global Mars atmosphere. *Journal of Geophysical Research*, *105*(E4), 9553–9571. https://doi.org/10.1029/1999JE001089

Coates, A. J., Jaumann, R., Griffiths, A. D., Leff, C. E., Schmitz, N., Josset, J. L., et al. (2017). The PanCam instrument for the ExoMars rover. *Astrobiology*, *17*(6–7), 511–541. https://doi.org/10.1089/ast.2016.1548

Davis, J. (2019). *CTX digital elevation models—Martian dunes*. figshare Collection. https://doi.org/10.6084/M9.FIGSHARE.C.4649537.V1

Davis, J. M., Banham, S. G., Grindrod, P. M., Boazman, S. J., Balme, M. R., & Bristow, C. S. (2020). Morphology, development, and sediment dynamics of elongating linear dunes on Mars. *Geophysical Research Letters*, e2020GL088456. https://doi.org/10.1029/2020GL088456

Davis, J. M., Grindrod, P. M., Boazman, S. J., Vermeesch, P., & Baird, T. (2020). Quantified Aeolian dune changes on Mars derived from repeat context camera images. *Earth and Space Science*, *7*, e2019EA000874. https://doi.org/10.1029/2019EA000874

Day, M., & Kocurek, G. (2016). Observations of an aeolian landscape: From surface to orbit in Gale Crater. *Icarus*, *280*, 37–71. https://doi.org/10.1016/j.icarus.2015.09.042

de Silva, S. L., Spagnuolo, M. G., Bridges, N. T., & Zimbelman, J. R. (2013). Gravel-mantled megaripples of the Argentinean Puna: A model for their origin and growth with implications for Mars. *GSA Bulletin*, *125*(11–12), 1912–1929.

Ehlmann, B. L., Edgett, K. S., Sutter, B., Achilles, C. N., Litvak, M. L., Lapotre, M. G. A., et al. (2017). Chemistry, mineralogy, and grain properties at Namib and High dunes, Bagnold dune field, Gale crater, Mars: A synthesis of Curiosity rover observations. *Journal of Geophysical Research: Planets*, *122*(12), 2510–2543. https://doi.org/10.1002/2017JE005267

Favaro, E. A., Grindrod, P., & (2020). *Oxia Planum ArcGIS and excel files Version 2*. The Open University. https://doi.org/10.21954/ou.rd.13042802.v2

Favaro, E. A., Hugenholtz, C. H., Barchyn, T. E., & Gough, T. R. (2020). Wind regime, sediment transport, and landscape dynamics at a Mars analogue site in the Andes Mountains of Northwestern Argentina. *Icarus*, *346*, 113765. https://doi.org/10.1016/j.icarus.2020.113765

Fawdon, P., Balme, M. R., Bridges, J., Davis, J. M., Gupta, S., & Quantan-Nataf, C. (2019). The ancient fluvial catchment of Oxia Planum: The Exomars 2020 rover landing site. In Lunar and Planetary Science Conference (Vol. 50). (p. 2356).

Fenton, L. K., Michaels, T. I., & Chojnacki, M. (2015). Late Amazonian aeolian features, gradation, wind regimes, and sediment state in the vicinity of the Mars Exploration Rover Opportunity, Meridiani Planum, Mars. *Aeolian Research*, *16*, 75–99.

Forget, F., Hourdin, F., Fournier, R., Hourdin, C., Talagrand, O., Collins, M., et al. (1999). Improved general circulation models of the Martian atmosphere from the surface to above 80 km. *Journal of Geophysical Research*, *104*(E10), 24155–24175.

Goetz, W., Pike, W. T., Hviid, S. F., Madsen, M. B., Morris, R. V., Hecht, M. H., et al. (2010). Microscopy analysis of soils at the Phoenix landing site, Mars: Classification of soil particles and description of their optical and magnetic properties. *Journal of Geophysical Research*, *115*(E8). https://doi.org/10.1029/2009JE003437

Grindrod, P. M., Hollingsworth, J., Ayoub, F., & Hunt, S. A. (2018). The search for active marsquakes using subpixel coregistration and correlation: Best practice and first results. *Journal of Geophysical Research: Planets*, *123*(7), 1881–1900. https://doi.org/10.1029/2018JE005649

Hayward, R. K., Fenton, L. K., & Titus, T. N. (2014). Mars Global Digital Dune Database (MGD3): Global dune distribution and wind pattern observations. *Icarus*, *230*, 38–46. http://dx.doi.org/10.1016/j.icarus.2013.04.011

He, K., Zhang, X., Ren, S., & Sun, J. (2016). Deep residual learning for image recognition. In *Proceedings of the IEEE conference on computer vision and pattern recognition* (pp. 770–778).

Holmes, J. A., Lewis, S. R., & Patel, M. R. (2020). OpenMARS: A global record of martian weather from 1999 to 2015. *Planetary and Space Science*, *188*, 104962. https://doi.org/10.1016/j.pss.2020.104962

Hoskins, B. J., & Simmons, A. J. (1975). A multi-layer spectral model and the semi-implicit method. *Quarterly Journal of the Royal Meteorological Society*, *101*(429), 637–655.
Hugenholtz, C. H., & Barchyn, T. E. (2017). A terrestrial analog for transverse aeolian ridges (TARs): Environment, morphometry, and recent dynamics. *Icarus*, *289*, 239–253.
Hugenholtz, C. H., Barchyn, T. E., & Favaro, E. A. (2015). Formation of periodic bedrock ridges on Earth. *Aeolian Research*, *18*, 135–144.
Jaumann, R., Neukum, G., Behnke, T., Duxbury, T. C., Eichentopf, K., Flohrer, J., et al. (2007). The high-resolution stereo camera (HRSC) experiment on Mars Express: Instrument aspects and experiment conduct from interplanetary cruise through the nominal mission. *Planetary and Space Science*, *55*(7–8), 928–952.
Josset, J. L., Westall, F., Hofmann, B. A., Spray, J., Cockell, C., Kempe, S., et al. (2017). The Close-Up Imager onboard the ESA ExoMars Rover: objectives, description, operations, and science validation activities. *Astrobiology*, *17*(6-7), 595–611. https://doi.org/10.1089/ast.2016.1546
Kerber, L., & Head, J. W. (2010). The age of the Medusae Fossae Formation: Evidence of Hesperian emplacement from crater morphology, stratigraphy, and ancient lava contacts. *Icarus*, *206*(2), 669–684. https://doi.org/10.1016/j.icarus.2009.10.001
Kirk, R. L., Howington-Kraus, E., Redding, B., Galuszka, D., Hare, T. M., Archinal, B. A., et al. (2003). High-resolution topomapping of candidate MER landing sites with Mars Orbiter Camera narrow-angle images. *Journal of Geophysical Research*, *108*(E12). https://doi.org/10.1029/2003JE002131
Kirk, R. L., Howington-Kraus, E., Rosiek, M. R., Anderson, J. A., Archinal, B. A., Becker, K. J., et al. (2008). Ultrahigh resolution topographic mapping of Mars with MRO HiRISE stereo images: Meter-scale slopes of candidate Phoenix landing sites. *Journal of Geophysical Research*, *113*(E3). https://doi.org/10.1029/2007je003000
Kleinböhl, A., Schofield, J. T., Kass, D. M., Abdou, W. A., Backus, C. R., Sen, B., et al. (2009). Mars Climate Sounder limb profile retrieval of atmospheric temperature, pressure, and dust and water ice opacity. *Journal of Geophysical Research*, *114*(E10). https://doi.org/10.1029/2009JE003358
Lapotre, M. G. A., Ewing, R. C., Lamb, M. P., Fischer, W. W., Grotzinger, J. P., Rubin, D. M., et al. (2016). Large wind ripples on Mars: A record of atmospheric evolution. *Science*, *353*(6294), 55–58. https://doi.org/10.1126/science.aaf3206
Lapotre, M. G. A., Ewing, R. C., Weitz, C. M., Lewis, K. W., Lamb, M. P., Ehlmann, B. L., et al. (2018). Morphologic diversity of Martian ripples: Implications for large-ripple formation. *Geophysical Research Letters*, *45*(19), 10–229.
LeCun, Y., Bengio, Y., & Hinton, G. (2015). Deep learning. *Nature*, *521*(7553), 436–444.
Leprince, S., Barbot, S., Ayoub, F., & Avouac, J. P. (2007). Automatic and precise orthorectification, coregistration, and subpixel correlation of satellite images, application to ground deformation measurements. *IEEE Transactions on Geoscience and Remote Sensing*, *45*(6), 1529–1558. https://doi.org/10.1109/TGRS.2006.888937
Lewis, S. R., Read, P. L., Conrath, B. J., Pearl, J. C., & Smith, M. D. (2007). Assimilation of thermal emission spectrometer atmospheric data during the Mars Global Surveyor aerobraking period. *Icarus*, *192*(2), 327–347.
Lorenc, A. C., Bell, R. S., & Macpherson, B. (1991). The Meteorological Office analysis correction data assimilation scheme. *Quarterly Journal of the Royal Meteorological Society*, *117*(497), 59–89.
Malin, M. C., Bell, J. F., Cantor, B. A., Caplinger, M. A., Calvin, W. M., Clancy, R. T., et al. (2007). Context camera investigation on board the Mars Reconnaissance Orbiter. *Journal of Geophysical Research*, *112*(E5). https://doi.org/10.1029/2006JE002808
Mandon, L., Parkes Bowen, A., Quantin-Nataf, C., Bridges, J. C., Carter, J., Pan, L., et al. (2020). High-resolution characterization of the clay-bearing unit at Oxia Planum, the ExoMars 2020 landing site. *LPI*, (2326), (p. 1114).
Mandt, K. E, de Silva, S. L., Zimbelman, J. R., & Crown, D. A. (2008). Origin of the Medusae Fossae Formation, Mars: Insights from a synoptic approach. *Journal of Geophysical Research*, *113*, E12011. https://doi.org/10.1029/2008JE003076
McCleese, D. J., Schofield, J. T., Taylor, F. W., Calcutt, S. B., Foote, M. C., Kass, D. M., et al. (2007). Mars Climate Sounder: An investigation of thermal and water vapor structure, dust and condensate distributions in the atmosphere, and energy balance of the polar regions. *Journal of Geophysical Research*, *112*(E5). https://doi.org/10.1029/2006JE002790
McNeil, J., Balme, M., Fawdon, P., & Coe, A. L. (2020). Morphology, Morphometry, and Distribution of Isolated Landforms on the Margin of Chryse Planitia, Mars, *Europlanet Science Congress*, EPSC2020-216.
Metzger, S. M., Balme, M. R., Towner, M. C., Bos, B. J., Ringrose, T. J., & Patel, M. R. (2011). In situ measurements of particle load and transport in dust devils. *Icarus*, *214*(2), 766–772. https://doi.org/10.1016/j.icarus.2011.03.013
Milana, J. P. (2009). Largest wind ripples on Earth? *Geology*, *37*(4), 343–346.
Milana, J. P., & Kröhling, D. M. (2017). First data on volume and type of deflated sediment from Southern Puna Plateau and its role as source of the Chaco-Pampean loess. *Quaternary International*, *438*, 126–140. https://doi.org/10.1016/j.quaint.2017.03.007
Molina, A., López, I., Prieto-Ballesteros, O., Fernández-Remolar, D., de Pablo, M. Á., & Gómez, F. (2017). Coogoon Valles, western Arabia Terra: Hydrological evolution of a complex Martian channel system. *Icarus*, *293*, 27–44. https://doi.org/10.1016/j.icarus.2017.04.002
Montgomery, D. R., Bandfield, J. L., & Becker, S. K. (2012). Periodic bedrock ridges on Mars. *Journal of Geophysical Research*, *117*(E3). https://doi.org/10.1029/2011JE003970
Newman, C. E., Lewis, S. R., Read, P. L., & Forget, F. (2002). Modeling the Martian dust cycle, 1. Representations of dust transport processes. *Journal of Geophysical Research*, *107*(E12), 6–1. https://doi.org/10.1029/2002JE001910
Pavlov, A. K., Blinov, A. V., & Konstantinov, A. N. (2002). Sterilization of Martian surface by cosmic radiation. *Planetary and Space Science*, *50*(7–8), 669–673.
Perrin, C., Rodriguez, S., Jacob, A., Lucas, A., Spiga, A., Murdoch, N. ., & Lognonné, P. (2020). Monitoring of dust devil tracks around the insight landing site, Mars, and comparison with in situ atmospheric data. *Geophysical Research Letters*, *47*(10), e2020GL087234. https://doi.org/10.1029/2020gl087234
Poulet, F., Gross, C., Horgan, B., Loizeau, D., Bishop, J. L., Carter, J., & Orgel, C. (2020). Mawrth Vallis, Mars: A Fascinating place for future in situ exploration. *Astrobiology*, *20*(2), 199–234.
Priestley, A. (1993). A quasi-conservative version of the semi-Lagrangian advection scheme. *Monthly Weather Review*, *121*(2), 621–629.
Quantin-Nataf, C., Carter, J., Mandon, L., Thollot, P., Balme, M., Volat, M., et al. (2020). Oxia Palnum—The landing site for the 2020 ExoMars 'Rosalind Franklin' Rover Mission: geological context and pre-landing interpretation. *Astrobiology*. https://doi.org/10.1089/ast.2019.2191
Raack, J., Reiss, D., Balme, M. R., Taj-Eddine, K., & Ori, G. G. (2018). In situ sampling of relative dust devil particle loads and their vertical grain size distributions. *Astrobiology*, *18*(10), 1305–1317. https://doi.org/10.1089/ast.2016.1544
Rafkin, S., Jemmett-Smith, B., Fenton, L., Lorenz, R., Takemi, T., Ito, J., & Tyler, D. (2016). Dust devil formation. *Space Science Reviews*, *203*(1–4), 183–207.

Read, P. L., Lewis, S. R., & Kass, D. M. (2017). The state of the Martian climateState of the Climate in 2016. *Bulletin of the American Meteorological Society*, *98*(8), S60–S62. https://doi.org/10.1175/2017BAMSStateoftheClimate.1

Reiss, D., Fenton, L., Neakrase, L., Zimmerman, M., Statella, T., Whelley, P., et al. (2016). Dust devil tracks. *Space Science Reviews*, *203*(1–4), 143–181.

Reiss, D., Raack, J., & Hiesinger, H. (2011). Bright dust devil tracks on Earth: implications for their formation on Mars. *Icarus*, *211*(1), 917–920.

Reiss, D., Spiga, A., & Erkeling, G. (2014). The horizontal motion of dust devils on Mars derived from CRISM and CTX/HiRISE observations. *Icarus*, *227*, 8–20.

Reiss, D., Zanetti, M., & Neukum, G. (2011). Multitemporal observations of identical active dust devils on Mars with the High Resolution Stereo Camera (HRSC) and Mars Orbiter Camera (MOC). *Icarus*, *215*(1), 358–369. https://doi.org/10.1016/j.icarus.2011.06.011

Runyon, K. D., Bridges, N. T., Ayoub, F., Newman, C. E., & Quade, J. J. (2017). An integrated model for dune morphology and sand fluxes on Mars. *Earth and Planetary Science Letters*, *457*, 204–212. https://doi.org/10.1016/j.epsl.2016.09.054

Silvestro, S., Chojnacki, M., Vaz, D. A., Cardinale, M., Yizhaq, H., & Esposito, F. (2020). Megaripple migration on Mars. *Journal of Geophysical Research: Planets*, *125*(8), e2020JE006446. https://doi.org/10.1029/2020JE006446

Silvestro, S., Vaz, D. A., Yizhaq, H., & Esposito, F. (2016). Dune-like dynamic of Martian aeolian large ripples. *Geophysical Research Letters*, *43*(16), 8384–8389. https://doi.org/10.1002/2016GL070014

Simmons, A. J., & Burridge, D. M. (1981). An energy and angular-momentum conserving vertical finite-difference scheme and hybrid vertical coordinates. *Monthly Weather Review*, *109*(4), 758–766.

Simonyan, K., & Zisserman, A. (2014). Very deep convolutional networks for large-scale image recognition. *In Proc. International Conference on Learning Representations*. arXiv preprint arXiv:1409.1556. http://arxiv.org/abs/1409.1556(2014)

Smith, M. D. (2004). Interannual variability in TES atmospheric observations of Mars during 1999–2003. *Icarus*, *167*(1), 148–165.

Smith, M. D., Pearl, J. C., Conrath, B. J., & Christensen, P. R. (2000). Mars Global Surveyor Thermal Emission Spectrometer (TES) observations of dust opacity during aerobraking and science phasing. *Journal of Geophysical Research*, *105*(E4), 9539–9552. https://doi.org/10.1029/1999JE001097

Squyres, S. W., Arvidson, R. E., Bollen, D., Bell III, J. F., Brueckner, J., Cabrol, N. A., et al. (2006). Overview of the opportunity mars exploration rover mission to meridiani planum: Eagle crater to purgatory ripple. *Journal of Geophysical Research: Planets*, *111*(E12), https://doi.org/10.1029/2010JE003746

Stanzel, C., Pätzold, M., Greeley, R., Hauber, E., & Neukum, G. (2006). Dust devils on Mars observed by the high resolution stereo camera. *Geophysical Research Letters*, *33*(11). https://doi.org/10.1016/j.icarus.2008.04.017

Stanzel, C., Pätzold, M., Williams, D. A., Whelley, P. L., Greeley, R., Neukum, G., & HRSC Co-Investigator Team. (2008). Dust devil speeds, directions of motion and general characteristics observed by the Mars Express High Resolution Stereo Camera. *Icarus*, *197*(1), 39–51. https://doi.org/10.1016/j.icarus.2008.04.017

Sullivan, R., Arvidson, R., Bell, J. F., III, Gellert, R., Golombek, M., Greeley, R., et al. (2008). Wind-driven particle mobility on Mars: Insights from Mars Exploration Rover observations at "El Dorado" and surroundings at Gusev Crater. *Journal of Geophysical Research: Planets*, *113*(E6). https://doi.org/10.1029/2008JE003101

Sullivan, R., Banfield, D., Bell, J. F., Calvin, W., Fike, D., Golombek, M., et al. (2005). Aeolian processes at the Mars exploration rover Meridiani Planum landing site. *Nature*, *436*(7047), 58–61.

Tanaka, K. L., Skinner, J. A., Jr., Dohm, J. M., Irwin, R. P., III, Kolb, E. J., Fortezzo, C. M., Platz, T., et al. (2014). Geologic map of Mars: U.S. *Geological Survey Scientific Investigations Map*, *3292*, 43. https://dx.doi.org/10.3133/sim3292

Thomas, N., Cremonese, G., Ziethe, R., Gerber, M., Brändli, M., Bruno, G., et al. (2017). The color and stereo surface imaging system (CaSSIS) for the ExoMars trace gas orbiter. *Space Science Reviews*, *212*(3–4), 1897–1944. https://doi.org/10.1007/s11214-017-0421-1

Thomas, P., Veverka, J., Lee, S., & Bloom, A. (1981). Classification of wind streaks on Mars. *Icarus*, *45*(1), 124–153. https://doi.org/10.1016/0019-1035(81)90010-5

Tsoar, H. (1989). Linear dunes—Forms and formation. *Progress in Physical Geography*, *13*(4), 507–528. https://doi.org/10.1177/030913338901300402

Vago, J. L., Spoto, F., & Bauer, M. (2018). *Oxia Planum favored for ExoMars surface mission*. European Space Agency. Retrieved from https://exploration.esa.int/web/mars/-/60914-oxia-planum-favoured-for-exomars-surface-mission

Vago, J. L., Westall, F., Coates, A. J., Jaumann, R., Korablev, O., Ciarletti, V., et al. (2017). Habitability on early Mars and the search for biosignatures with the ExoMars Rover. *Astrobiology*, *17*(6–7), 471–510.

Vago, J., Witasse, O., Svedhem, H., Baglioni, P., Haldemann, A., Gianfiglio, G., et al. (2015). ESA ExoMars program: the next step in exploring Mars. *Solar System Research*, *49*(7), 518–528.

Weitz, C. M., Sullivan, R. J., Lapotre, M. G., Rowland, S. K., Grant, J. A., Baker, M., & Yingst, R. A. (2018). Sand grain sizes and shapes in eolian bedforms at Gale Crater, Mars. *Geophysical Research Letters*, *45*(18), 9471–9479. https://doi.org/10.1029/2018GL078972

Zimbelman, J. R. (2010). Transverse aeolian ridges on Mars: First results from HiRISE images. *Geomorphology*, *121*(1–2), 22–29.